

Spin Dynamics Simulations of Composite Radical Pairs as Magnetic Compass Sensors



Nathan Clark
Keble College

A thesis submitted for the Honour School of Chemistry

Part II 2022

Acknowledgements

Firstly, I would like to thank Professor Peter Hore FRS who has been extremely supportive and welcoming throughout the Part II Year. Peter has been an exceptional supervisor and I feel very fortunate to have worked and learnt from him. I promise you I will learn how to spell cyrptochrome.

I would like to extend my thanks to other members of the Hore group: Pip, Yi, Gediminas, Rachel and Alice. I have enjoyed working alongside all of you and thank you for making my brief stint in the group such an enjoyable one. I would like to emphasise my thanks to Yi for the provision of many tasty lunches and for teaching me how to use chopsticks, Pip for help with the writing of my thesis, Gediminas for answering all of my questions and to Alice for providing support with spinach.

I am extremely thankful to Max for the significant number of insightful conversations over the course of the year, I hate to think what my thesis would have looked like without your insight. I think you are owed a trip to the tapas restaurant.

Many thanks to Gareth, Tim, Max and Sam for making 103 such a nice place to live.

Thank you Grace helping with my thesis and making for such an enjoyable year.

I am grateful for the support provided by all of my college tutors over the past four years, especially Dr Thomas Player for the support you provided and for inspiring to join the Hore group, which I am very grateful for.

Finally, I would like to thank my family for all of their support.

Summary

In 1822, a white stork was found injured with an African hunting spear lodged through its neck near the German village of Klütz [1] (Figure 1), providing the first evidence of birds undergoing long-distance migrations.

Since this discovery, some species of birds have been shown to detect the direction of the Earth's magnetic field, enabling such navigational abilities [3–5]. The leading hypothesis behind the magnetic compass sense is the radical pair mechanism (RPM). The RPM relies on the magnetically-sensitive spin dynamics of a pair of spin-correlated radicals, which react spin-selectively to give products whose yields vary with the direction and strength of the Earth's magnetic field [6].

To date, the only plausible biological compass sensor is a cryptochrome protein [6]. However, measurements made by Xu *et al.* [7] show that an altered (mutant) cryptochrome is more sensitive to magnetic fields than the wild-type protein under *in vitro* conditions. This appears to be inconsistent with an optimised magnetic compass sensor and raises questions as to why evolution would have resulted in a sub-optimal magnetic compass sensor [7].

This observation has led to the suggestion that the RPM in cryptochromes is not based on a single radical pair (RP), but that a second RP is involved to allow for the optimisation of both the signalling and sensing functions of the magnetoreceptor,



Figure 1: The *Rostocker Pfeilstorch*, Figure reproduced from [2].

in order to provide the most effective magnetic compass sense [7]. Wong *et al.* demonstrated in [8] that the two-site RP system can be modelled as a single ‘composite’ RP, with weighted average properties [7].

Using spin dynamics calculations of the cryptochrome system as a two-site (composite) RP compass sensor, this thesis investigates why the mutant protein is more sensitive than the wild-type cryptochrome *in vitro*.

This is done by introducing avian magnetoreception in migratory birds (chapter 1) and the theoretical background required to model the physics of cryptochrome photochemistry (chapter 2).

chapter 3 describes the methods for calculating reaction yields in the cryptochrome system. It also assesses these approaches with the aim of producing the most realistic simulations possible by balancing the number of data points and nuclear-spins included with the inclusion/exclusion of spin relaxation.

Finally, chapter 4 uses spin dynamics calculations to provide an answer to the apparent inconsistency found by Xu *et al.* in [7], that the mutant protein is more sensitive to applied magnetic fields than the wild-type cryptochrome *in vitro*.

The work carried out in chapter 4 also leads to additional findings which suggest that the two-site (composite) RP in the cryptochrome is, to date, the most suitable magnetic compass sensor for migratory birds. This suggestion is due to evidence that the cryptochrome magnetic compass sensor can gain a boost in sensitivity by adopting a two-site (composite) RPM, over one with a single-site RP (conventional/mutant RPM), due to the greater flexibility in rate constants that can be achieved. Also, it is shown that adoption of the (two-site) composite RPM over the previously accepted [6] (one-site) conventional RPM leads to an increase in the value of the optimal forward rate constant to a more physically reasonable one. It was also explained why the composite nature of the RP is limited to the inclusion of Trp_C and Trp_D.

Contents

1	Introduction	1
1.1	Avian Magnetoreception	1
1.2	Magnetite Hypothesis	3
1.3	Radical Pair Mechanism	4
1.3.1	Spin	4
1.3.2	Reaction Scheme	5
1.4	Composite-Radical Pair Mechanism	10
1.5	Aims of This Project	15
2	Theoretical Background	16
2.1	Matrix Representation	16
2.1.1	Basis Sets and Representations	17
2.1.2	Spin-1/2 Particles	17
2.1.3	Multi-Spin Operators	18
2.1.4	Expectation Values	18
2.1.5	Density Matrix	19
2.1.6	Projection Operators	21
2.1.7	Singlet Product Yield	22
2.1.8	Liouville Space	22
2.2	Spin Hamiltonian	23
2.2.1	Zeeman Interaction	23
2.2.2	Hyperfine Interaction	24
2.2.3	Dipolar Coupling	25
2.2.4	Exchange Coupling	25
3	Modelling Techniques	26
3.1	Composite Model	27
3.2	Reaction Kinetics	28
3.3	Compass Sensitivity	29
3.4	Hilbert Space Calculation of Singlet Yield	30
3.5	Relaxation	32
3.6	Liouville Space Calculation of Singlet Yield	33
3.7	The Flavin-Tryptophan Radical Pair	34

3.8	Evaluation of Methods	35
3.8.1	Results	36
3.8.2	Number of Points	36
3.8.3	Number of Spins	38
3.8.4	Inclusion of Relaxation	39
4	Validity of the Composite-Radical Pair Mechanism	43
4.1	Five Nuclear-Spin System	43
4.2	Higher-Spin Systems	49
4.3	Why Four Tryptophans Instead of Three?	51
4.4	Validity of Rate Constant Condition	52
4.5	Possibility of Expanding the Composite Model to Include Trp-B . .	53
4.6	Conclusions	53
5	Conclusions and Future Work	55
	Bibliography	57
	Appendices	
A	Hyperfine and Dipolar Tensors	62
A.1	Hyperfine Tensors	62
A.2	Dipolar Tensors	62
B	Mutant RPM Figure	64

Chapter 1

Introduction

Contents

1.1	Avian Magnetoreception	1
1.2	Magnetite Hypothesis	3
1.3	Radical Pair Mechanism	4
1.3.1	Spin	4
1.3.2	Reaction Scheme	5
1.4	Composite-Radical Pair Mechanism	10
1.5	Aims of This Project	15

1.1 Avian Magnetoreception

The European robin migrates thousands of miles each year, from breeding grounds in Northern Europe to Africa during the autumn, before returning during the spring to secure better environmental conditions. The ability of robins and other young migratory birds to navigate such distances alone on their first autumn migration demonstrates the innate nature of such abilities [5, 6, 9], which has fascinated scientists and non-scientists alike.

This fascination has lead to a significant research effort to uncover the mechanism(s) behind such an ability. Since the 1960s, it has been known that birds are able to detect the Earth's magnetic field [3, 4], which has lead to the hypothesis of a magnetic compass sense in night migratory birds (avian magnetoreception).

Migratory birds are known to use a host of navigational cues, which are thought to be integrated together to provide a successful toolkit for navigation [5]. These cues involve celestial compasses, olfaction and landmarks, which have different levels of importance during the various stages of migration. Avian magnetoreception is thought to be vital during the long-distance phase, along with the celestial compass ability and use of landmarks such as coastlines [5].

Avian magnetoreception is believed to be comprised of a magnetic compass and map, with the map developed over multiple migrations. Both the magnetic compass and map are required for true navigation [5], in which they independently provide directional and geographical information. This requirement can be realised by the need for humans to have both a compass and map prior to the use of GPS.

Experiments uncovering key details about the nature of the magnetic sense have given insights into the mechanism(s) behind it. These experiments have shown that the magnetic compass used by migratory birds is an inclination compass which uses the angle between the Earth's magnetic field lines and its surface [10–12]. This is different to a traditional polarity compass which can distinguish the North and South Poles using a small magnet that is attracted to one Pole and repelled by the other. It has been reported that birds can detect magnetic field vectors with an accuracy better than 5° [13, 14].

Studies have also shown that the compass is activated by blue light, with a wavelength of about 565nm, as the birds seem to calibrate their compass at sunset when significant amount of light of this wavelength is available [6]. Both of these observations along with the disorientation of migratory birds in the presence of electromagnetic fields [15–19] are characteristic of the involvement of quantum mechanical effects in the mechanism behind avian magnetoreception. Avian magnetoreception remains one of the most significant unsolved problems in sensory biology.

The two most promising mechanisms by which avian magnetoreception is believed

to occur will now be discussed. Firstly, the magnetite hypothesis, followed by the radical pair mechanism (RPM).

1.2 Magnetite Hypothesis

Magnetite (Fe_3O_4) chains are found in magnetotactic bacteria and lead to magnetically orientated swimming behaviour [20–22]. Single-domain magnetite particles are rotated into alignment with the Earth’s magnetic field, which in the bacterium’s case, results in a passive alignment with the Earth’s magnetic field. It has been hypothesised that this action of the single-domain particles could transmit a signal to the brain forming the basis of an intensity or direction sensor in migratory birds [23]. Currently no such chains of magnetite have been detected in the tissues of birds or other vertebrates [20–22].

A growing body of evidence suggests that the ophthalmic branch of the trigeminal nerve (V1), the only nonolfactory nerve entering the upper beak, is involved in magnetoreception [6]. Several studies in which V1 had been surgically severed showed significant effects on the birds’ abilities to detect magnetic field changes [24]. However, the magnetic information carried by the V1 nerve is unlikely to provide compass information due to intact trigeminal nerves not being necessary for magnetic-compass orientation [25,26]. Rather, V1 is likely to provide magnetic map information. This was demonstrated by surgical severing the V1 nerves in migratory reed warblers. They were still able to sense magnetic fields, use their magnetic compass sense, but were no longer capable of adjusting for the 1,000-km magnetic displacements that they are otherwise capable of [27].

In conclusion, the magnetite hypothesis is unlikely to be the mechanism behind the magnetic compass sense, of which this thesis is concerned. However, it has the potential to form the apparent magnetic map in the beaks of migratory birds, such as reed warblers [6].

1.3 Radical Pair Mechanism

The radical pair mechanism was first suggested as the basis for avian magnetoreception by Schulten in 1978 [28, 29]. This is due to the radical pair mechanism (and a few rare variants) being the only known possible way in which weak magnetic fields ($B \ll \frac{k_B T}{\hbar \gamma_e}$) can affect the outcome of chemical reactions [30], due to the radical pair being far enough from thermal equilibrium that thermal control is irrelevant [6]. This allows for small interactions, dependent on the magnetic field, to have a significant impact on the singlet-triplet interconversion (step 3 in Figure 1.1) and consequently, the outcome of the reaction.

To describe the radical pair mechanism, and hence the magnetic field's effect, a pair of coupled electron spins must be considered. Therefore, an introduction of spin and coupled states is required.

1.3.1 Spin

In 1922, Stern and Gerlach demonstrated that electrons possess an internal non classical degree of freedom [31], an internal angular momentum, "spin". By analogy to other kinds of angular momentum, spin can be fully described by two quantum numbers: s , the spin quantum number and m_s , the spin projection (magnetic) quantum number.

These quantum numbers relate to the eigenvalues of states $|s, m_s\rangle$, which are simultaneous eigenstates of \hat{S}^2 (the total squared spin angular momentum operator) and \hat{S}_z (the operator corresponding to the z -component of the spin angular momentum).

$$\hat{S}^2|s, m_s\rangle = \hbar^2 s(s+1)|s, m_s\rangle \quad s \in \left\{0, \frac{1}{2}, 1, \frac{3}{2}, \dots\right\} \quad (1.1)$$

$$\hat{S}_z|s, m_s\rangle = \hbar m_s|s, m_s\rangle \quad m_s \in \{-s, -s+1, \dots, s-1, s\} \quad (1.2)$$

Unlike classical angular momentum, which results from an object spinning about an axis, s can take a half-integer value (Equation 1.1). This demonstrates the intrinsic

nature of spin and differentiates it from other forms of angular momentum.

Another important property of spin is that it must be conserved during chemical reactions, unless there is spin-orbit coupling to allow for the conservation of the overall angular momentum.

Coupled States - Radical Pair Spin States

Two electron spins can couple according the Clebsch-Gordan series to form coupled states. These states can be described by the quantum numbers S , the total spin angular momentum and M_S , the total spin projection quantum number.

$$S = s_1 + s_2, s_1 + s_2 - 1, \dots |s_1 - s_2| \quad (1.3)$$

$$M_S = -S, -S + 1, \dots, S - 1, S \quad (1.4)$$

Therefore, the two eigenstates for a pair of electrons $|\frac{1}{2}, \frac{1}{2}\rangle$ and $|\frac{1}{2}, -\frac{1}{2}\rangle$, referred to as $|\alpha\rangle$ and $|\beta\rangle$, respectively make up a set of four states when coupled. There are three $S = 1$, triplet (T), states with $M_S = 0, \pm 1$:

$$|T_{+1}\rangle = |1, 1\rangle = |\alpha\alpha\rangle \quad (1.5)$$

$$|T_0\rangle = |1, 0\rangle = \frac{1}{\sqrt{2}}(|\alpha\beta\rangle + |\beta\alpha\rangle) \quad (1.6)$$

$$|T_{-1}\rangle = |1, -1\rangle = |\beta\beta\rangle \quad (1.7)$$

and a $S = 0$, singlet (S), state with $M_S = 0$:

$$|S\rangle = |0, 0\rangle = \frac{1}{\sqrt{2}}(|\alpha\beta\rangle - |\beta\alpha\rangle) \quad (1.8)$$

These states will be continuously referred back to when discussing the radical pair mechanism and its variants.

1.3.2 Reaction Scheme

Figure 1.1 is an example radical pair (RP) reaction scheme that could form the basis of a magnetic compass sensor in migratory birds [30].

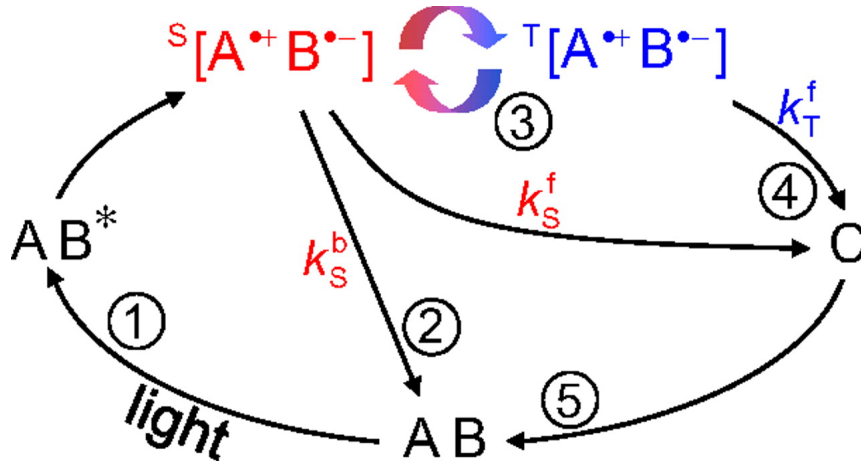


Figure 1.1: Example reaction scheme of a photocycle behind the radical pair mechanism, reproduced from [30]. Step 1 is the formation of a spin-correlated radical pair (RP) via photoexcitation. Step 2 is the recombination of the singlet state (red) of the RP back to the ground state with a rate constant of k_S^b . Step 3 (the blue and red curved arrows) depicts singlet-triplet interconversion between the singlet (red) and triplet (blue) states of the spin-correlated radical pair. Step 4 is the protonation of the singlet and triplet states in the spin-correlated radical pair to form the product C, with rate constants k_S^f and k_T^f , respectively.

The first step of the RPM is the formation of a spin-correlated radical pair (RP), which can occur via a number of different mechanisms. For this discussion it has been assumed that the radical pair is formed via the photoexcitation of the chemical species B, which has then undergone an electron transfer with A (Step 1 in Figure 1.1). For the purposes of this thesis the radical pair has been chosen to be formed in the singlet state as $^S[A^{\bullet+}B^{\bullet-}]$ (red), due to the biological system studied.

The next step, Step 3 in Figure 1.1, is the magnetically sensitive singlet-triplet interconversion of the spin-correlated radical pair. This interconversion is allowed due to the hyperfine (subsection 2.2.2) and Zeeman (subsection 2.2.1) interactions, which break the spin selection rule, causing the singlet and triplet states to be non-stationary spin-states. Therefore, the radical pair oscillates coherently between singlet and triplet states, modulated by the magnetic field strength and direction (if the hyperfine interactions are anisotropic).

The routes out of the radical pair differ for singlet and triplet states, allowing for the product yields to be influenced by applied magnetic fields due to their

impact on the proportion of singlet and triplet states in the radical pair. The singlet state can undergo spin selective recombination back the ground state, Step 2 in [Figure 1.1](#), which is forbidden for the triplet state due to the requirement for the conversion of spin. The two radicals can also undergo protonation to produce the same product C, Steps 4 in [Figure 1.1](#).

Therefore, if the yields of different products can be measured, the RPM can form the basis of a magnetically sensitive chemical compass.

For a system to be suitable as a magnetic compass, the following conditions must be met [32]: 1. The radicals must be at least partially-immobilized to detect the direction of an external magnetic field. 2. The radicals must remain spin-correlated for enough time ($\geq 1\mu s$) for the applied (Earth’s) magnetic field to have a significant effect on the reaction yields. 3. The radicals must possess magnetic nuclei so that hyperfine driven singlet-triplet interconversion will take place. 4. The radicals must be well-separated so that the electron-electron and spin-spin interactions are not much stronger than the hyperfine coupling or the external magnetic field. 5. k_T^f should be close enough to k_S^f and k_S^b so that there is sufficient competition between singlet and triplet products, such that one pathway does not dominate.

Experimental Evidence

As mentioned, the radical pair mechanism is, to date, the only mechanism known to be influenced by weak magnetic fields. Therefore, due to the Earth’s weak magnetic field ($25 - 60 \mu T$) [33], the RPM is the only chemical mechanism that is a contender. The previously mentioned light-dependence of avian magnetoreception [6] is consistent with the RPM and provides confidence in the mechanism.

The nature of the magnetic compass sense being inclination-based as opposed to polarity-based [10–12] is also consistent with a RPM due to the symmetry of the RP interactions under the time-reversal operator; it can be shown that

the fractional yield of the RP reaction is also invariant under the inversion of an external magnetic field [34].

Further evidence for the RPM as the basis of avian magnetoreception has been provided by the design of a poof-of-principle RP magnetoreceptor (Figure 1.2), which has been shown to be sensitive, *in vitro*, to low magnetic fields and their direction [35].

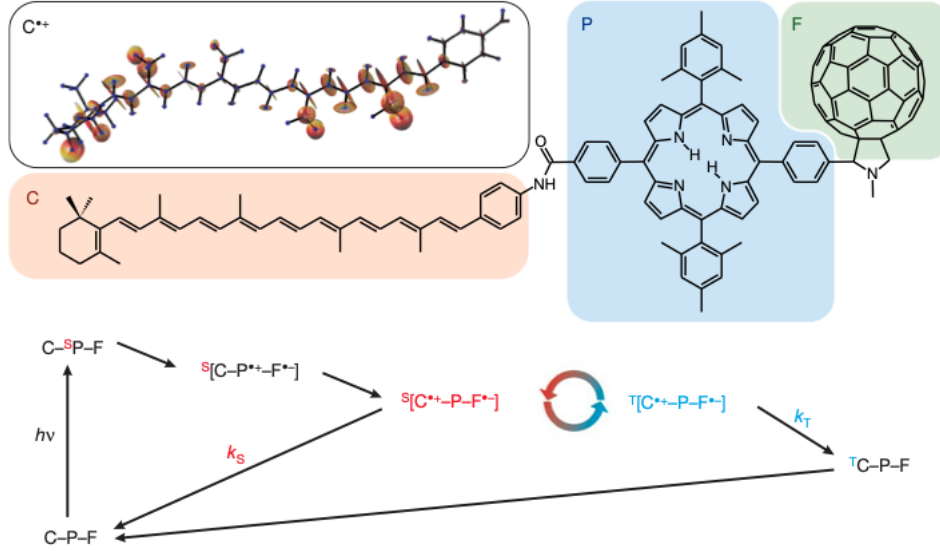


Figure 1.2: Structure (top) and reaction scheme (bottom) of the C-P-F triad, carotenoid (C) and fullerene (F) separated by a porphyrin (P) linker, used to demonstrate the principle of a chemical magnetic compass, reproduced from [35]. In the reaction scheme, the singlet and triplet spin-selective reactions of the spin-correlated radical pair occur with the rate constants k_S and k_T , respectively. $h\nu$ represents the excitation of the ground state C-P-F triad to form the spin correlated radical pair $^{S/T}[\text{C}^{\bullet+}\text{-P-F}^{\bullet-}]$ (singlet/triplet).

The most substantial evidence for the RPM is the disorientation observed in birds when weak time-dependent radiofrequency fields are applied [15–19], because it seemingly rules out the magnetite hypothesis. Magnetite particles large enough to align with the Earth’s magnetic field would be too large to be affected by such small fields, however, the RPM is believed to be sensitive enough to be affected [6].

Computational Evidence

Computational studies have provided insight into the RPM and the effect different parameters have on the overall signal of the compass [6]. They are essential in combination with experimental data to understand the processes behind avian

magnetoreception. In addition, the insight from simulations aids the design of new experiments.

Magnetic Field Effect

The magnetic field effect (MFE) on the product yield can be quantified. Figure 1.3 shows the variation of singlet product yield Φ_s with the applied magnetic field strength B , for a RP with hyperfine coupling to a single ^1H nuclei in one of the radicals (single-proton RP).

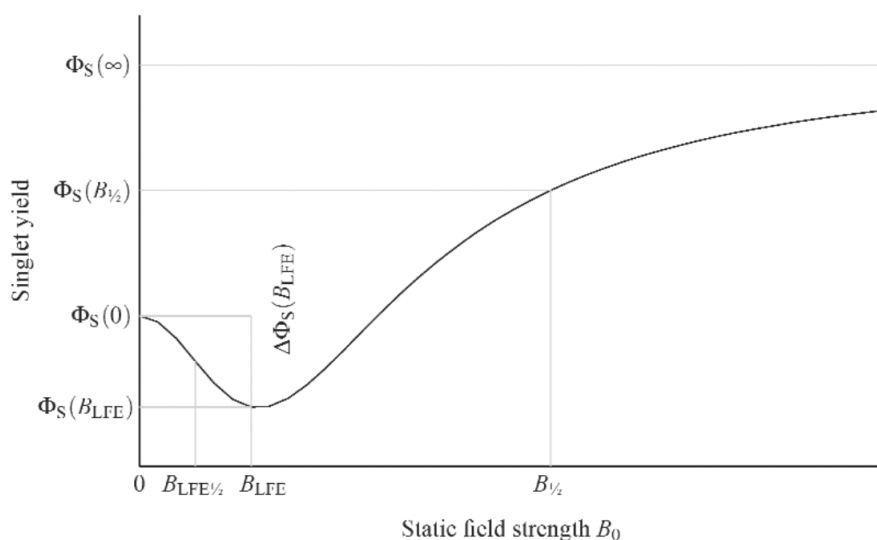


Figure 1.3: Singlet product yield Φ_s against static field strength B for a RP with hyperfine coupling to a single ^1H nuclei in one of the radicals (single-proton RP). The figure has been reproduced from [36].

At high magnetic fields the Zeeman interaction (subsection 2.2.1) causes a large singlet-triplet separation which reduces singlet-triplet mixing. The reduced singlet-triplet mixing results in slower singlet to triplet interconversion, leading to an increased singlet yield. This high-field relationship is known as the normal MFE.

The opposite relationship is seen at low fields, known as the low field effect (LFE). LFE arises due to the lifting of some, or all, the energy-level degeneracies that occur in the absence of a magnetic field. This acts to unblock zero-frequency coherences, which allows them to evolve, leading to more singlet-triplet interconversion and

consequentially triplet product formation. Therefore, for the single-proton case, LFE causes a reduction in the singlet yield [37].

Under the Earth's magnetic field strength of $25 - 65 \mu\text{T}$ [33], that migratory birds experience, the important magnetic field effect is the LFE.

1.4 Composite-Radical Pair Mechanism

In order to discuss the radical pair mechanism in migratory birds, it is vital to mention the site at which it is believed to take place.

Cryptochrome

To date, the only plausible magnetoreceptor for migratory birds is a cryptochrome protein found in the retina [6]. Since the 2000s, cryptochromes have been suggested as a possible candidate [38] and have provided tangibility to the radical pair hypothesis as a mechanism behind avian magnetoreception. Numerous studies have been carried out and have identified Cry4 as the most likely magnetoreceptor [7, 39].

Cryptochrome are blue-light sensitive photoreceptors and it is believed that Cry4, depicted in Figure 1.4, undergoes a RPM at sunset when there is sufficient blue light to form a significant amount of the spin-correlated radical pair [6]. The product yields are expected to vary based on the direction and location of the bird, due to the variation in the strength and direction of the Earth's magnetic field. The amount of product formed is believed to correspond to the extent at which a conformational change at the C-terminus of the Cry4 occurs [40], which could result in a signal sent to the brain for the bird to use as navigational information [40].

Molecular dynamics simulations have shown that the electron transfer chain in *ErCry4a* and *ClCry4a* have a very similar structure and distance between key components [7]. Therefore, Figure 1.4 can be used as a general picture of Cry4 for migratory birds.

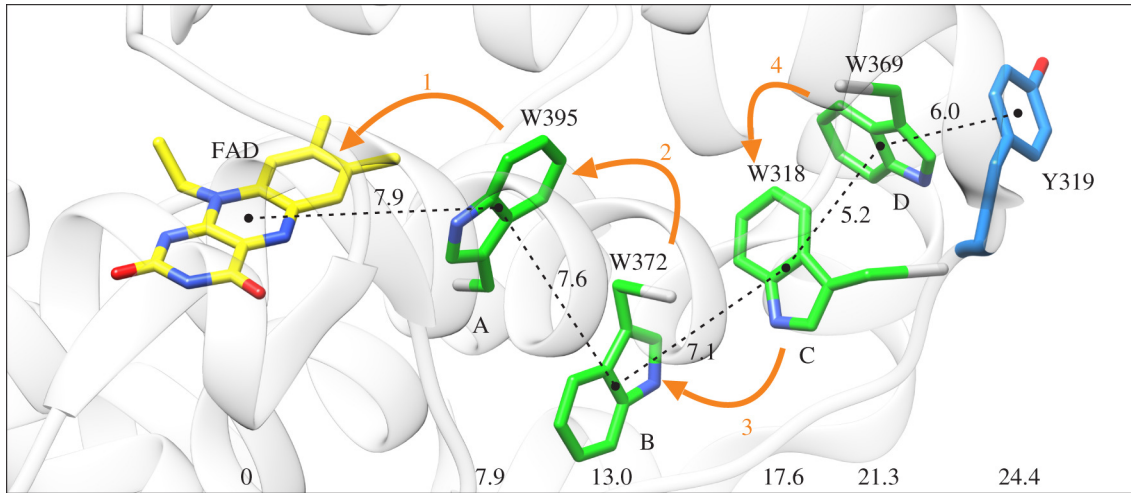


Figure 1.4: Structure of the electron transfer chain in the pigeon (*Columba livia*, *Cl*) Cry4a. Shown is the flavin component (yellow) of the flavin adenine dinucleotide (FAD) cofactor, the Tyr319 (blue) residue is labelled Y319 and the four tryptophans (W) (green), labelled: A (W395), B (W372), C (W318) and D (W369). All distances are given in Å (from [41]) and the orange arrows represent the four sequential electron transfers. The figure has been reproduced from [8].

Work carried out by Xu *et al.* [7] made several significant findings. It was the first study to make measurements of purified Cry4 for a migratory bird *in vitro*, there are no *in vivo* measurements of Cry4.

Xu *et al.* reported that the migratory European robin (*Erithacus rubecula*, *Er*) Cry4 is significantly more sensitive to magnetic fields than the non-migratory pigeon Cry4 and chicken Cry4. This is supportive of Cry4 as the site of the magnetic compass, as the migratory European robin is expected to have experienced greater evolutionary pressure to optimise its magnetic compass sense than non-migratory birds.

Xu *et al.* also made four mutants, W_xF ($x = A, B, C, D$), in which each tryptophan (W) was replaced with a phenylalanine (F), at site x (Figure 1.4), to block electron transfer at different points along the chain. Blue light irradiation of the W_AF , W_BF and W_CF mutants failed to yield radicals with a lifetime long enough to be magnetically sensitive. Measurements of radical-radical separations of the wild-type (WT) and W_DF mutant clearly showed that $RP1_D$ is the dominant transient charge-separated state in the WT protein [7].

Measurements made by Xu *et al.* showed that the WT protein is less sensitive to magnetic fields than the mutant, $W_D F$, *in vitro* [7]. This raises the question posed by Wong *et al* in [8] regarding Cry4 as a magnetic compass sensor, as to why migratory birds have evolved to have a four tryptophans (Trp) instead of three. The assumption here is that evolutionary pressure would lead to the system optimising the magnetic compass sense in order to boost chances of survival. Therefore, as there are examples of Cry4 with three tryptophans in nature such as in the plant *Arabidopsis thaliana*, which clearly does not migrate, this finding is inconsistent with a system optimised to act as a magnetic compass [7, 8].

Suggestions have been made that the answer to this apparent inconsistency may come from a modified RPM, where there are contributions from the RP on both Trp_C and Trp_D [7]. The reasoning for this suggestion is that evolutionary pressure could have developed Cry4 to be capable as both a sensing and a signalling protein, so as to be the most efficient possible biological magnetic compass. Therefore, if *in vivo* the RP on Trp_C ($RP1_C$) is more sensitive than the RP on Trp_D ($RP1_D$) (as in the case *in vitro*), whilst $RP1_D$ is more efficient at signalling, the system could be optimised by fast reversible interconversion between $RP1_C$ and $RP1_D$.

$RP1_D$ is believed to be better at signalling than $RP1_C$ due to two main reasons: Firstly, due to the closeness of $RP1_D$ to the surface of the cryptochrome compared to $RP1_C$ (Figure 1.4), making $RP1_D$ better placed to generate a signalling state due to the greater accessibility of the proton involved in the forward deprotonation step [7, 8]. Secondly, due to $RP1$'s close proximity to the Tyr319 residue 3.7Å away (Figure 1.4) [41–43], which may reduce $Trp_D H^{\bullet+}$ (in $RP1_D$) to allow for the efficient formation of a signalling state, with $FADH^{\bullet}$ as the only radical [8].

Electron Transfer Rates

The key assumption behind the optimisation of sensing and signalling functions is that RP1_C and RP1_D interconvert by fast-reversible electron hopping [7]. Figure 1.5 shows the approximate rate constants of the electron transfer reactions in the European robin Cry4 (*ErCry4*) [7].

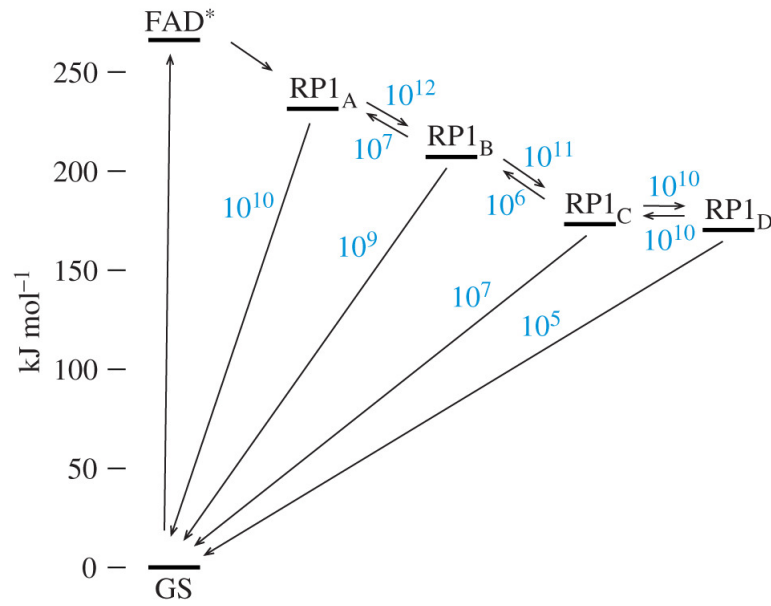


Figure 1.5: Approximate rate constants (s^{-1}) for electron transfer reactions in *ErCry4*. GS represents the ground state. This figure has been reproduced from [8].

From Figure 1.5 it is clear that the interconversion between RP1_C and RP1_D is significantly faster than singlet-triplet interconversion ($\approx 10^6 \text{ s}^{-1}$) [6], or any reaction out of RP1_C or RP1_D . This implies that both radical pairs may contribute to the magnetic compass sense. Therefore, a modified (two-site) reaction scheme can be considered, with interconverting RPs, where one of the electrons resides on the FAD and the other on Trp_C or Trp_D to give RP1_C and RP1_D , respectively (Figure 1.6 (b)).

Reaction Scheme

Wong *et al.* showed that the two-site model RPM depicted in Figure 1.6 (b) can be reliably reduced to a one-site (composite) RPM (Figure 1.6 (a)), when the rate of interconversion (k_{CD} and k_{DC}) is $\geq 10^{10} \text{ s}^{-1}$ (Figure 1.7) [8]. As the rate of

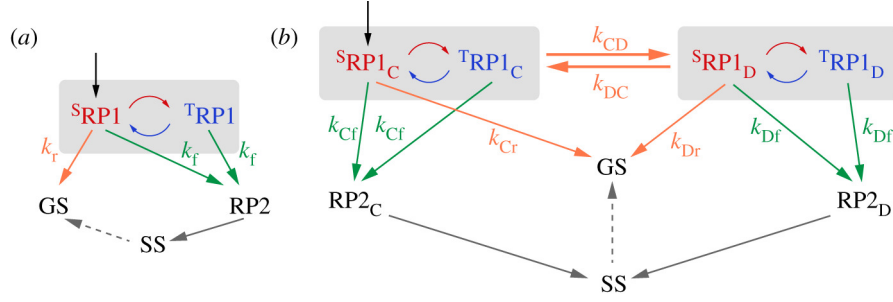


Figure 1.6: (a) Magnetic field effects on the yield of the signalling state (SS) come from a single radical pair, RP1 (section 1.3). Where $RP1 = RP1_C, RP1_D$, or a weighted average of the two for the mutant RPM, conventional RPM and composite, respectively. GS is the ground state, S and T are the singlet and triplet states. k_r and k_f are the recombination and forward rate constants, respectively. (b) two-site RPM where both $RP1_C$ and $RP1_D$ contribute to the magnetic field effect (section 1.4). GS is the ground state of the protein. The relevant rate constants are labelled by k with a subscript denoting the process involved. r for recombination, f for forward and C or D for the radical pair involved. Figure 1.6 is reproduced from [8]

interconversion in *ErCry* is predicted to be 10^{10} s^{-1} (Figure 1.5), the composite RPM is suitable to be used throughout this thesis to model the system. In the composite RPM, the two interconverting radical pairs are treated as a single entity with weighted average properties [8]. This drastically reduces the computational demands of modelling the spin dynamics of the system and will be discussed further in chapter 3.

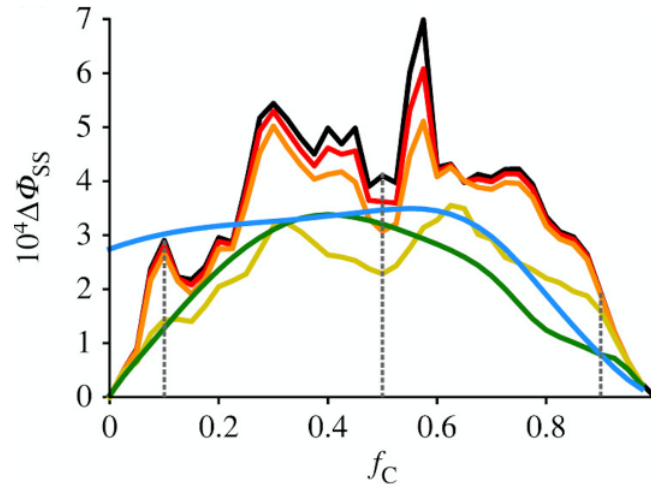


Figure 1.7: Singlet Yield Anisotropy plotted against the fraction of RPs in the $RP1_C$ state (f_C). The black line is made by using the composite RPM. The rest use a two-site, non-composite, model and have the following interconversion rates (in s^{-1}): red 3×10^{10} , orange 10^{10} , yellow 10^9 , green 10^8 and blue 10^7 . All calculations are made with five-nuclear-spin case (section 3.7) and have a relaxation constant of 10^6 s^{-1} . There is no reason to think that this relationship will not hold for more nuclear spins or for a different relaxation constant. This figure has been reproduced from [8].

1.5 Aims of This Project

The results presented in this thesis will be broken down into three main sections:

1. In [chapter 2](#) the essential background required to model the photochemistry of the cryptochrome will be introduced.
2. The assessment of modeling techniques for composite RP systems applied to magnetic compass sensing ([chapter 3](#))
3. The possibility of the involvement of Trp_C via the composite RPM as a potential magnetic compass sensor to assess the suggested answers to the inconsistencies found by Xu *et al.* in [7] ([chapter 4](#)).

Chapter 2

Theoretical Background

Contents

2.1	Matrix Representation	16
2.1.1	Basis Sets and Representations	17
2.1.2	Spin-1/2 Particles	17
2.1.3	Multi-Spin Operators	18
2.1.4	Expectation Values	18
2.1.5	Density Matrix	19
2.1.6	Projection Operators	21
2.1.7	Singlet Product Yield	22
2.1.8	Liouville Space	22
2.2	Spin Hamiltonian	23
2.2.1	Zeeman Interaction	23
2.2.2	Hyperfine Interaction	24
2.2.3	Dipolar Coupling	25
2.2.4	Exchange Coupling	25

As stated in [chapter 1](#), the aim of this thesis is to gain a better understanding of the mechanism behind avian magnetoreception using computational simulations. Firstly, this chapter will introduce the framework required to model the system, before discussing the relevant interactions in the system and their representations.

2.1 Matrix Representation

This section will introduce the machinery required to describe the spin-dynamics of the radical pair (RP).

2.1.1 Basis Sets and Representations

Quantum mechanics describes systems in terms of quantum states, elements of a Hilbert space (\mathcal{H}), that operators act upon. A computer can only work with numbers, not abstract Hilbert spaces. Therefore, a suitable computer-friendly representation must be formulated.

This can be done assuming the knowledge of an ortho-normal basis $\{|i\rangle\}_i$ of the Hilbert space, with a scalar product of $\langle i|j\rangle = \delta_{i,j}$ [44]. For any operator \hat{A} acting on a Hilbert space use of the completeness relation ($\sum_i |i\rangle\langle i| = \mathbb{1} \forall |i\rangle \in \mathcal{H}$) twice gives Equation 2.1.

$$\hat{A} = \mathbb{1} \cdot \hat{A} \cdot \mathbb{1} = \sum_i |i\rangle\langle i| \cdot \hat{A} \cdot \sum_j |j\rangle\langle j| = \sum_{i,j} \langle i|\hat{A}|j\rangle |i\rangle\langle j| \quad (2.1)$$

Defining a numerical matrix \mathbf{A} with elements $A_{i,j} = \langle i|\hat{A}|j\rangle \in \mathbb{C}$ enables the re-writing of Equation 2.1 as Equation 2.2.

$$\hat{A} = \sum_{i,j} A_{i,j} |i\rangle\langle j| \quad (2.2)$$

The same process can be carried out with a state vector $|\psi\rangle$.

$$|\psi\rangle = \mathbb{1} \cdot |\psi\rangle = \sum_i |i\rangle\langle i| \cdot |\psi\rangle = \sum_i \langle i|\psi\rangle |i\rangle \quad (2.3)$$

Defining a numerical vector $\vec{\psi}$ with elements $\langle i|\psi\rangle \in \mathbb{C}$ enables the re-writing of Equation 2.3 as Equation 2.4.

$$|\psi\rangle = \sum_i \psi_i |i\rangle \quad (2.4)$$

Both the matrix \mathbf{A} and the vector $\vec{\psi}$ are complex-valued objects which can be used in any computer system. Equation 2.2 and Equation 2.4 allow for any operator or state vector to be represented in a form that a computer can recognise and manipulate.

2.1.2 Spin-1/2 Particles

Spin and coupled states were introduced in subsection 1.3.1. A matrix representation is needed to model the relevant spin dynamics of the radical pairs computationally.

Matrix Representation

The Pauli Matrices, defined in Equation 2.5, form a basis for the vector space of 2×2 Hermitian matrices. Therefore, they can be used to build the matrix representation of the spin-1/2 operators that describe the spin dynamics of the system.

$$\sigma_x = \begin{pmatrix} 0 & 1 \\ 1 & 0 \end{pmatrix}, \sigma_y = \begin{pmatrix} 0 & -i \\ i & 0 \end{pmatrix}, \sigma_z = \begin{pmatrix} 1 & 0 \\ 0 & -1 \end{pmatrix}, \quad (2.5)$$

Use of Equation 1.2 along with the Pauli matrices allows for the formation of the spin projection operators (Equation 2.6).

$$\hat{S}_x = \frac{\hbar}{2}\sigma_x, \hat{S}_y = \frac{\hbar}{2}\sigma_y, \hat{S}_z = \frac{\hbar}{2}\sigma_z \quad (2.6)$$

Following the convention of this field, the spin operators, and by consequence all derived quantities, will be written in units of angular frequency, i.e. with $\hbar = 1$.

The analogous matrices can be formed for a particle of any spin quantum number.

2.1.3 Multi-Spin Operators

For a system of more than one spin, the spin projection operators can be built by taking the Kronecker products of the spin projection operator representing each individual spin in the system (Equation 2.7).

$$\hat{S}_i = \bigotimes_{j=1}^n \hat{s}_{i,j} \quad (2.7)$$

Where there are n spins in the system, \hat{S}_i and $\hat{s}_{i,j}$ are the spin projection operators for the multi-spin system and the single spin i , respectively. If all of the spins are spin- $\frac{1}{2}$ the dimensions of the total spin operator will be $\prod_{i=1}^n (2s_i + 1)$.

2.1.4 Expectation Values

For any operator \hat{A} the expectation value, $\langle \hat{A} \rangle$, of that observable A can be written as:

$$\langle \hat{A} \rangle = \langle \psi | \hat{A} | \psi \rangle \quad (2.8)$$

Where $|\psi\rangle$ is the normalised total wavefunction, such that $\langle\psi|\psi\rangle = 1$.

Every wavefunction can be written as a linear combination of orthonormal basis functions, $|i\rangle$, with coefficients, c_i , that represent the contribution from each basis function.

$$\psi = \sum_i c_i |i\rangle \quad (2.9)$$

Substitution of Equation 2.9 into Equation 2.8 gives Equation 2.10.

$$\langle\hat{A}\rangle = \sum_{i,j} c_i c_j^* \langle i|\hat{A}|j\rangle \quad (2.10)$$

Where, as shown in subsection 2.1.1, $\langle i|\hat{A}|j\rangle$ can be written as elements of a matrix \mathbf{A} .

$$\langle\hat{A}\rangle = \sum_{i,j} c_i c_j^* A_{ij} \quad (2.11)$$

All of the quantities in Equation 2.11 are numerical. Therefore, a computer can use Equation 2.11, which is derived from quantum mechanics, to work out the expected value of any observable.

2.1.5 Density Matrix

So far, only isolated spin systems have been considered; a method is required to treat macroscopic systems. To a good approximation the spin systems do not interact, so the macroscopic system can be treated as a large ensemble of isolated spin systems. The method used and introduced below is the density matrix formalisation.

For a pure state, in which all of the spin systems of the ensemble are in the same state, the density operator, $\hat{\rho}$, is defined as in Equation 2.12.

$$\hat{\rho} = |\psi\rangle\langle\psi| \quad (2.12)$$

An example of a pure state is the radical pair at time $t = 0$, in which all of the spin states are in the singlet state.

Use of Equation 2.9 allows for Equation 2.12 to be rewritten as Equation 2.13.

$$\hat{\rho} = |\psi\rangle\langle\psi| = \sum_{i,j} c_i c_j^* |i\rangle\langle j| \quad (2.13)$$

It is useful to define the corresponding density matrix $\boldsymbol{\rho}$ with elements ρ_{ij} .

$$\rho_{ij} = \langle i|\hat{\rho}|j\rangle = c_i c_j^* \quad (2.14)$$

If the system exists as a mixed state, a weighted mixture of pure states [45], only the probability that the system is in a particular state can be given [46]. Here, the density operator must be interpreted as an average for the system and expressed as:

$$\hat{\rho} = \sum_k p^k |\psi^k\rangle\langle\psi^k| \quad \text{Where} \quad \sum_k p^k = 1 \quad (2.15)$$

An example of a mixed state is an ensemble at thermal equilibrium. Or the radical pair at a time $t \geq 0$. The overbar that is used represents the weighted average.

Use of Equation 2.9 allows for Equation 2.15 to be rewritten as Equation 2.16.

$$\hat{\rho} = \sum_{i,j} \overline{c_i c_j^*} |i\rangle\langle j| = \overline{|\psi\rangle\langle\psi|} \quad (2.16)$$

For a mixed state the corresponding density matrix $\boldsymbol{\rho}$ has matrix elements ρ_{ij} .

$$\rho_{ij} = \langle i|\hat{\rho}|j\rangle = \overline{c_i c_j^*} \quad (2.17)$$

The diagonal elements of the density matrix, in the eigenbasis of the spin Hamiltonian, represent probability of being in that state. The off-diagonal elements in the eigenbasis of the spin Hamiltonian represent the so called coherences [47].

Expectation Values

Using the definition of the density matrix and Equation 2.11, the expectation value of an observable can be written as the trace of the matrix product of the density matrix with the matrix representation of the operator corresponding to that observable.

$$\langle \hat{A} \rangle = \sum_{ij} \rho_{ij} A_{ij} = \sum_{jj} (\boldsymbol{\rho} \mathbf{A})_{jj} = \text{Tr}(\boldsymbol{\rho} \mathbf{A}) = \text{Tr}(\mathbf{A} \boldsymbol{\rho}) \quad (2.18)$$

Time Dependence

Finding how the system evolves over time is a vital part of spin dynamics calculations.

This can be done using the definition of the density matrix and the product rule.

$$\frac{d}{dt}\hat{\rho}(t) = \frac{d|\psi(t)\rangle\langle\psi(t)|}{dt} = \frac{d|\psi(t)\rangle}{dt}\langle\psi(t)| + |\psi(t)\rangle\frac{d\langle\psi(t)|}{dt} \quad (2.19)$$

The next step is to make use the time-dependent Schrodinger [Equation 2.20](#).

$$\frac{d}{dt}|\psi(t)\rangle = -i\hat{H}(t)|\psi(t)\rangle \quad (2.20)$$

In order to re-write [Equation 2.19](#) as [Equation 2.21](#).

$$\frac{d}{dt}\hat{\rho}(t) = -i[\hat{H}(t), \hat{\rho}(t)] \quad (2.21)$$

The equation above is known as the Liouville-von Neumann equation and is of central importance to calculating the spin-dynamics of quantum mechanical systems [\[46\]](#).

[Equation 2.21](#) can be solved for a time-dependent Hamiltonian. However, there is a simple solution for a time-independent Hamiltonian considered in this thesis.

$$\hat{\rho}(t) = \hat{U}(t)\hat{\rho}(0)\hat{U}^\dagger(t) \quad (2.22)$$

Where $\hat{U}(t) = e^{-i\hat{H}t}$ is the propagator and $\hat{\rho}(0)$ is the initial density operator. All of these quantities can be modelled in a computer using the before mentioned methods.

2.1.6 Projection Operators

Projection operators have the following form

$$\hat{P}_j = \frac{|j\rangle\langle j|}{\langle j|j\rangle} \quad (2.23)$$

The projection operator, \hat{P}_j , projects an arbitrary state, $|\psi\rangle$, onto a specific state, $|j\rangle$, to give a coefficient c_j that represents the amount of $|j\rangle$ contained in $|\psi\rangle$.

$$\hat{P}_j|\psi\rangle = \sum_i c_i |j\rangle \frac{\langle j|i\rangle}{\langle j|j\rangle} = c_j |j\rangle \quad (2.24)$$

The singlet projection operator, \hat{P}_s , for a system with Z nuclear spin states is defined in Equation 2.25. It is used to calculate the singlet product yield, allowing for the monitoring of magnetic field effects, making it useful in this thesis.

$$\hat{P}_s = |S\rangle\langle S| \otimes \hat{1}_Z \quad (2.25)$$

N.B. $\langle S|S\rangle = 1$ as the basis states are orthonormal.

2.1.7 Singlet Product Yield

As discussed in chapter 1 the product yields of radical pair reactions can be altered by the strength and direction of the Earth's magnetic field. The definition of the singlet projection operator, \hat{P}_s , (Equation 2.25) can be used to express the singlet product yield Φ_s :

$$\Phi_s = k_r \int_0^\infty P_s(t) dt \quad (2.26)$$

where, k_r is the rate constant for the recombination of singlet radical pairs back to the singlet ground state. Φ_s is the fractional yield corresponding to the amount of the ground state that is reformed during the reaction.

2.1.8 Liouville Space

To involve non-coherent processes such as spin-spin relaxation, Liouville space is required [46]. Hilbert space is spanned by a basis of orthogonal wave functions, whereas Liouville space is spanned by a basis of orthogonal operators. The Hilbert space $n \times n$ density operators are row-wise flattened to form $n^2 \times 1$ operator vectors, $|\hat{\rho}(t)\rangle$, which are acted upon by $n^2 \times n^2$ superoperators. A Hilbert space of dimensions $n \times n$ corresponds to a $n^2 \times n^2$ Liouville operator space.

Superoperators

$\hat{\hat{H}}$ is the commutation superoperator which corresponds to the Hamiltonian.

$$\hat{\hat{H}} = \hat{H} \otimes \hat{1} - \hat{1} \otimes \hat{H}^T \quad (2.27)$$

$\hat{\mathbb{1}}$ is the identity superoperator which corresponds to the identity operator.

$$\hat{\mathbb{1}} = \hat{\mathbb{1}} \otimes \hat{\mathbb{1}} \quad (2.28)$$

Liouville-von Neumann Equation

The Liouville-von Neumann equation given in [Equation 2.21](#) in Hilbert space becomes:

$$\frac{d}{dt}|\hat{\rho}(t)\rangle = -i\hat{H}(t)|\hat{\rho}(t)\rangle \quad (2.29)$$

Which, for a time independent Hamiltonian, has the following solution:

$$|\hat{\rho}(t)\rangle = \exp(-i\hat{H}t)|\hat{\rho}(0)\rangle \quad (2.30)$$

2.2 Spin Hamiltonian

The total Hamiltonian operator for a molecular system is highly complicated. Fortunately, in Spin Chemistry it is sufficient to consider only the spin part of the Hamiltonian as would be done in NMR or ESR [\[46\]](#). The total spin Hamiltonian (\hat{H}) can be written as a sum of all of the relevant contributions that are described below:

$$\hat{H} = \hat{H}_{Zeeman} + \hat{H}_{HFI} + \hat{H}_{Dipolar} + \hat{H}_{Exchange} \quad (2.31)$$

2.2.1 Zeeman Interaction

As the electrons in the radical pair possess spin (intrinsic angular momentum), they generate a magnetic dipole moment, $\boldsymbol{\mu}$.

$$\boldsymbol{\mu} = \gamma_e \mathbf{S} \quad (2.32)$$

γ_e is the gyro-magnetic ratio for a free electron and \mathbf{S} is the spin angular-momentum of the free electron. When an external magnetic field (\mathbf{B}) is applied, a Zeeman interaction occurs, which acts to change the energy of the states with $M_s \neq 0$. This interaction is described by the relevant Hamiltonian (\hat{H}_{Zeeman}).

$$\hat{H}_{Zeeman} = -\boldsymbol{\mu} \cdot \mathbf{B} = -\gamma_e \mathbf{S} \cdot \mathbf{B} \quad (2.33)$$

Throughout this thesis $\mathbf{B} = B_0 (\sin \theta \cos \phi, \sin \theta \sin \phi, \cos \theta)^T$. \hat{H}_{Zeeman} becomes:

$$\hat{H}_{Zeeman} = -\gamma_e B_0 (\hat{S}_x \sin \theta \cos \phi + \hat{S}_y \sin \theta \sin \phi + \hat{S}_z \cos \theta) \quad (2.34)$$

γ_e has been assumed to be equal to that of a free electron. This is because the system only involves organic radicals, in which spin-orbit coupling is small [48].

The nuclear Zeeman interactions are more than an order of magnitude smaller than any other interaction included in the calculations in this thesis. This is due to the small gyro-magnetic ratios of nuclei. As a result, nuclear Zeeman interactions have been ignored.

2.2.2 Hyperfine Interaction

The tryptophan and flavin molecules that make up the radical pair in the cryptochrome, discussed in [chapter 1](#), contain magnetic nuclei (^1H , $S = \frac{1}{2}$) and (^{14}N , $S = 1$) which couple to the electron spins in the radical pair. These interactions are known as hyperfine interactions which are known to be made up of two components: the isotropic part that arises from Fermi contact interactions [46], in which the electrons are in contact with the nucleus that it is interacting with, in addition to the anisotropic part, due to through-space dipole-dipole interactions between the electrons and nearby nuclear-spins [46].

The Hamiltonian describing hyperfine coupling (\hat{H}_{HFI}) between an electron j and the nucleus k has the form:

$$\hat{H}_{HFI} = \hat{S}_j \cdot \mathbf{A}_{jk} \cdot \hat{I}_k \quad (2.35)$$

Where \mathbf{A}_{jk} is the hyperfine coupling tensor and \hat{S}_j and \hat{I}_k are the electron and nuclear spin operators, respectively.

Hyperfine interactions are crucial as they act to break down the spin selection rule of $\Delta S = 0$. This allows the hyperfine interactions to drive the coherent quantum-mechanical process of singlet-triplet interconversion. This is the process by which

the Earth's magnetic field impacts the product yields out of the radical pair. This is evident due to oscillations between singlet and triplet states occurring at frequencies determined by the strengths of hyperfine interactions [48].

The hyperfine tensors used in this thesis have been calculated by DFT and can be found in [Appendix A](#).

2.2.3 Dipolar Coupling

Dipolar coupling arises due from a through space dipole-dipole interaction of the electron spins in the radical pair. For two electrons, A and B, the associated Hamiltonian ($\hat{H}_{Dipolar}$) can be written as:

$$\hat{H}_{Dipolar} = \hat{S}_A \cdot \mathbf{D} \cdot \hat{S}_B \quad (2.36)$$

\mathbf{D} is the dipolar coupling tensor which scales with r^{-3} , where r is the distance between the interacting electrons. The dipolar interaction has a significant impact on the system so is included in all calculations throughout this thesis [7].

2.2.4 Exchange Coupling

Exchange coupling is between the two electrons, A and B, in the radical pair and is a result of the Pauli exclusion principle. It changes the energies of the singlet and triplet states with the form:

$$\hat{H}_{Exchange} = -J \hat{S}_A \cdot \hat{S}_B \quad (2.37)$$

Where J is the exchange constant that varies exponentially with the separation of the electrons. Due to the exponential variation of the exchange interaction with the separation between the electrons in the radical pair, the exchange interaction term has no significant impact on the calculations in this thesis [7]. Therefore, the exchange interaction has been ignored.

Chapter 3

Modelling Techniques

Contents

3.1	Composite Model	27
3.2	Reaction Kinetics	28
3.3	Compass Sensitivity	29
3.4	Hilbert Space Calculation of Singlet Yield	30
3.5	Relaxation	32
3.6	Liouville Space Calculation of Singlet Yield	33
3.7	The Flavin-Tryptophan Radical Pair	34
3.8	Evaluation of Methods	35
3.8.1	Results	36
3.8.2	Number of Points	36
3.8.3	Number of Spins	38
3.8.4	Inclusion of Relaxation	39

A difficult balancing act when designing spin dynamics calculations for biological systems is the trade-off between the validity of the simulations versus the CPU time and memory requirements of those simulations. The three main components of this balancing act are: 1. the amount of data generated, 2. the number of nuclear-spins included and 3. the inclusion/exclusion of spin relaxation. This chapter will assess what is necessary in order to make spin dynamics calculations as valid as possible with the available machinery. Firstly, the methods used to model the composite RPM in Hilbert and Liouville space will be introduced. The results and demands of these simulations will then be discussed.

3.1 Composite Model

In this chapter and the next, the cryptochrome system introduced in [section 1.4](#) is modelled.

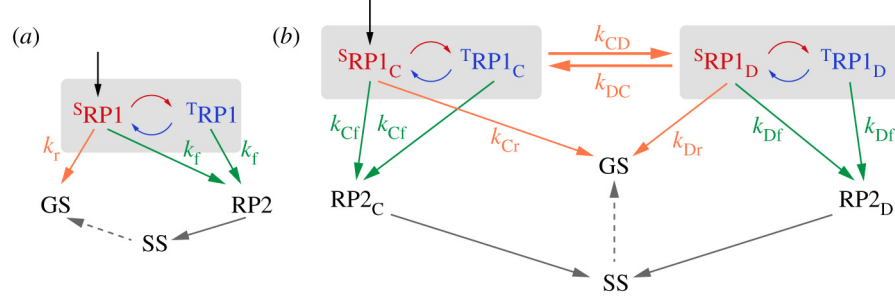


Figure 3.1: (a) Magnetic field effects on the yield of the signalling state (SS) come from a single radical pair, RP1 ([section 1.3](#)). Where $RP1 = RP1_C$, $RP1_D$, or a weighted average of the two for the mutant RPM, conventional RPM and composite, respectively. GS is the ground state, S and T are the singlet and triplet states. k_r and k_f are the recombination and forward rate constants, respectively. (b) two-site RPM where both $RP1_C$ and $RP1_D$ contribute to the magnetic field effect ([section 1.4](#)). GS is the ground state of the protein. The relevant rate constants are labelled by k with a subscript denoting the process involved. r for recombination, f for forward and C or D for the radical pair involved. [Figure 1.6](#) is reproduced from [8]

For clarity, the mutant, conventional and composite radical pair mechanisms are distinguished below:

1. The mutant RPM is a reference to the RPM with the mutant W_DF species produced and studied by Xu *et al.* in [7], where the system is made up of a single RP with an unpaired electron on Trp_C . This mechanism is represented by [Figure 3.1](#)

(a) where $RP1$ is $RP1_C$.

2. The conventional RPM is analogous to the mutant RPM, with the system consisting of a single RP with an unpaired electron on Trp_D . The conventional RPM is a reference to the conventionally accepted RPM behind the wild type cryptochrome in Nature. This mechanism is represented by [Figure 3.1](#) (a) where $RP1$ is $RP1_D$.

3. The composite RPM can be represented by [Figure 3.1](#) (a), with a system consisting of two rapidly interconverting RPs that behave as a single weighted average ‘composite’ RP. In the composite RPM $RP1$ is made up by contributions

from both $RP1_C$ and $RP1_D$.

In the composite RPM, f_C and f_D are the proportions of $RP1_C$ and $RP1_D$ that make up the transient charge-separated RP (RP1) in the cryptochrome. The values of f_C and f_D are related as shown in Equation 3.1 [7, 8], where k_{CD} and k_{DC} are the rate constants for interconversion between $RP1_C$ and $RP1_D$.

$$\frac{f_C}{f_D} \equiv \frac{k_{DC}}{k_{CD}} \text{ and } f_C + f_D \equiv 1 \quad (3.1)$$

Using Equation 3.1, the quantities describing the composite system can be written as a weighted average, made up of contributions from both $RP1_C$ and $RP1_D$. The spin Hamiltonian for the composite radical pair, $\hat{H}_{\langle RP1 \rangle}$, is made up of contributions from both \hat{H}_{RP1_C} and \hat{H}_{RP1_D} .

$$\hat{H}_{\langle RP1 \rangle} = f_C \hat{H}_{RP1_C} + f_D \hat{H}_{RP1_D} \quad (3.2)$$

The same method is followed to define the composite dipolar interaction tensor, \mathbf{D} (Equation 3.3), and the composite rate constants, k_f and k_r (Equation 3.4). \mathbf{D}_C and \mathbf{D}_D can be found in section A.2.

$$\mathbf{D} = f_C \mathbf{D}_C + f_D \mathbf{D}_D \quad (3.3)$$

Where, \mathbf{D}_C and \mathbf{D}_D are the dipolar tensors for $RP1_C$ and $RP1_D$, respectively.

$$k_f = f_C k_{Cf} + f_D k_{Df} \text{ and } k_r = f_C k_{Cr} + f_D k_{Dr} \quad (3.4)$$

Where, k_{Cf} and k_{Df} are the forward rate constants from $RP1_C$ and $RP1_D$, respectively, and k_{Cr} and k_{Dr} are their singlet recombination counterparts (Figure 3.1).

3.2 Reaction Kinetics

To model the spin dynamics depicted in Figure 3.1 the introduction of a kinetics operator (\hat{K}), which accounts for chemical reactions of the radical pair is required. This thesis will use the conventional phenomenological Haberkorn recombination

operator [49]. For the composite reaction scheme in Figure 3.1 (a) \hat{K} takes the following form

$$\hat{K}\hat{\rho} = \frac{k_r}{2} [\hat{P}_s, \hat{\rho}]_+ + k_f [\hat{\mathbb{1}}, \hat{\rho}]_+ \quad (3.5)$$

where \hat{P}_s is the singlet projection operator, defined in Equation 2.25, $\hat{\rho}$ is the density operator defined in Equation 2.15 and the ‘ $_+$ ’ denotes an anti-commutator. The analogous superoperator ($\hat{\hat{K}}$) can be formed as:

$$\hat{\hat{K}}\hat{\rho} = \frac{k_r}{2} [\hat{P}_s \otimes \hat{\mathbb{1}} + \hat{\mathbb{1}} \otimes (\hat{P}_s)^T] + k_f \hat{\mathbb{1}} \quad (3.6)$$

There has been debate over the validity of the phenomenological Haberkorn approach in recent years [50–53]. However, studies have shown that the difference between the two excepted models: Haberkorn [49] and Jones-Hore [50], is non-detectable and purely theoretical apart from in rare cases [50, 54].

3.3 Compass Sensitivity

In order to monitor the effects that conditions have on the magnetic compass sense it is important to have a marker of sensitivity for the compass. As mentioned in chapter 1 and chapter 2 product yields of the radical pair reaction can be altered by the direction of the Earth’s magnetic field. For the composite RPM (Figure 3.1) the signalling state yield, Φ_{ss} , is defined by Equation 3.7. It is clear that $\Phi_{RP1C} + \Phi_{RP1D} + \Phi_s \equiv 1$ must be true where, Φ_{RP1C} and Φ_{RP1D} represent the product yields of the forward reaction out of their respective radical pairs. Φ_s is the singlet recombination product yield as defined in Equation 2.26.

$$\Phi_{ss} = \Phi_{RP1C} + \Phi_{RP1D} = 1 - \Phi_s \quad (3.7)$$

The singling state anisotropy, $\Delta\Phi_{ss}$, can be calculated using Equation 3.8.

$$\Delta\Phi_{ss} = \max_{\theta, \phi}(\Phi_{ss}) - \min_{\theta, \phi}(\Phi_{ss}) \quad (3.8)$$

Where the maximum and minimum values of the signalling state yield (Φ_{ss}) are determined by sampling a large number of geomagnetic field directions (θ, ϕ).

The singling state anisotropy ($\Delta\Phi_{ss}$) gives a measure of the sensitivity of the magnetic compass sense to the direction of the Earth's magnetic fields. Therefore, $\Delta\Phi_{ss}$ will be used as the measure of compass sensitivity in this thesis, following the method used by Wong *et al* [8].

In [section 3.4](#) and [section 3.6](#) the methods used to calculate Φ_s in Hilbert and Liouville space will be introduced. [Equation 3.7](#) and [Equation 3.8](#) can then be used to relate Φ_s to $\Delta\Phi_{ss}$.

3.4 Hilbert Space Calculation of Singlet Yield

The inclusion of reaction kinetics in Hilbert space modifies the Liouville-von Neumann equation ([Equation 2.21](#)) that describes the spin dynamics of the system to

$$\frac{d}{dt}\hat{\rho}(t) = -i[\hat{H}, \hat{\rho}(t)]_- - [\hat{K}, \hat{\rho}(t)]_+ \quad (3.9)$$

Where \hat{H} and \hat{K} are time-independent and $[\dots]_-$ and $[\dots]_+$ represent commutators and anti-commutators, respectively. By defining $\hat{\gamma} = \hat{H} - i\hat{K}$ as the total operator for the spin dynamics of the system [Equation 3.9](#) can be re-written as [Equation 3.10](#).

$$\frac{d}{dt}\hat{\rho}(t) = -i\hat{\gamma}\hat{\rho}(t) + i\hat{\rho}(t)\hat{\gamma}^\dagger \quad (3.10)$$

It is important to note that $\hat{\gamma}$ is non-Hermitian. [Equation 3.10](#) can be solved to give the solution shown in [Equation 3.11](#).

$$\hat{\rho}(t) = \exp(-i\hat{\gamma}t)\hat{\rho}(0)\exp(+i\hat{\gamma}^\dagger t) \quad (3.11)$$

From now on I will switch to matrix representations for clarity. Let $\mathbf{A}^{-1}\boldsymbol{\gamma}\mathbf{A} = \mathbf{y}$ where \mathbf{y} is the diagonal matrix of eigenvalues of $\boldsymbol{\gamma}$ in the eigenbasis of the Hamiltonian. We can see that the eigendecompositions of $\boldsymbol{\gamma}$ and $\boldsymbol{\gamma}^\dagger$ are related:

$$(\mathbf{A}^{-1}\boldsymbol{\gamma}\mathbf{A})^\dagger = \mathbf{A}^\dagger\boldsymbol{\gamma}^\dagger(\mathbf{A}^{-1})^\dagger = \mathbf{y}^\dagger = \mathbf{y}^* \quad (3.12)$$

Equation 3.11 can be used along with the relation in Equation 2.18 to calculate the probability of being in the singlet state at a given time, t , $\mathbf{P}_s(t)$.

$$\mathbf{P}_s(t) = \text{Tr} [\boldsymbol{\rho}(t) \mathbf{P}_s] = \text{Tr} [\exp(-i\boldsymbol{\gamma}t) \boldsymbol{\rho}(0) \exp(+i\boldsymbol{\gamma}^\dagger t) \mathbf{P}_s] \quad (3.13)$$

Identity relations can be used to manipulate Equation 3.13 to Equation 3.14.

$$\mathbf{P}_s(t) = \text{Tr} [\mathbf{A} \mathbf{A}^{-1} \exp(-i\boldsymbol{\gamma}t) \mathbf{A} \mathbf{A}^{-1} \boldsymbol{\rho}(0) (\mathbf{A}^{-1})^\dagger \mathbf{A}^\dagger \exp(+i\boldsymbol{\gamma}^\dagger t) (\mathbf{A}^{-1})^\dagger \mathbf{A}^\dagger \mathbf{P}_s] \quad (3.14)$$

Using the fact that matrices can be cyclicly permuted within a trace and the definitions of \mathbf{y} and \mathbf{y}^* allows rearrangement of Equation 3.14 to Equation 3.15.

$$\mathbf{P}_s(t) = \text{Tr} [\exp(-i\mathbf{y}t) \mathbf{A}^{-1} \boldsymbol{\rho}(0) (\mathbf{A}^{-1})^\dagger \exp(+i\mathbf{y}^*t) \mathbf{A}^\dagger \mathbf{P}_s \mathbf{A}] \quad (3.15)$$

All of the radical pairs are formed in the singlet state. Therefore, $\boldsymbol{\rho}(0) = \frac{1}{Z} \mathbf{P}_s$ where Z is the number of nuclear spin states. Substitution of this along with the definition of $\mathbf{B} = \mathbf{A}^{-1} \mathbf{P}_s (\mathbf{A}^{-1})^\dagger$ and $\mathbf{C} = \mathbf{A}^\dagger \mathbf{P}_s \mathbf{A}$ allows for re-writing of Equation 3.15 as Equation 3.16.

$$\begin{aligned} \mathbf{P}_s(t) &= \frac{1}{Z} \text{Tr} [\exp(-i\mathbf{y}t) \mathbf{B} \exp(+i\mathbf{y}^*t) \mathbf{C}] \\ &= \frac{1}{Z} \sum_{j,k=1}^{4Z} B_{jk} C_{kj} e^{i(y_{kk}^* - y_{jj})t} \end{aligned} \quad (3.16)$$

Use of Equation 3.16, Equation 2.26 and the standard integral of $\int_0^\infty e^{ixt} dt = \frac{i}{x}$ (for $\text{Im}(x) > 0$), allows for the calculation of Φ_s as:

$$\Phi_s = \frac{ik_r}{Z} \sum_{j,k=1}^{4Z} \frac{B_{jk} C_{kj}}{y_{kk}^* - y_{jj}} \quad (3.17)$$

There are expressions for Φ_s that are much less computationally demanding than derived above. However, they require the neglect of dipolar interactions or the use of symmetric rate constants. Unfortunately, dipolar interactions have a significant impact on $\Delta\Phi_{SS}$ so they have to be included. Furthermore, the cryptochrome composite RP can not be modelled with symmetric rate constants ($k_f \equiv k_r$), because singlet and triplet RP states react spin selectively. The singlet state undergoes both recombination and the forward reaction, unlike the triplet state which only undergoes the forward reaction (Figure 3.1).

3.5 Relaxation

Spin relaxation is essential for accurate spin dynamics calculations due to it being the most significant problem with the RPM [6, 8]. Relaxation acts to bring the population of nuclear spin states towards thermal equilibrium, i.e. with 25% in the singlet state and 75% in the triplet states. Therefore, spin relaxation leads to a reduction in the Earth's magnetic field's ability to impact product yields. This causes a reduction in the signalling state anisotropy ($\Delta\Phi_{ss}$), reducing the sensitivity of the magnetic compass sense.

Since spin relaxation can not be modelled in Hilbert space, Liouville space must be used [46]. This is because the spin relaxation operator for the system is non-diagonalisable in Hilbert space. Liouville space is a mathematical trick that transforms the system into a solvable one, at the cost of increased dimensions.

In this thesis the random fields model is used in order to introduce spin relaxation via the spin relaxation superoperator \hat{W} [55].

$$\hat{W} = k_{relax} \left\{ \frac{3}{2} \hat{\mathbb{1}} - \sum_{i \in \{FAD, W\}} \sum_{j \in \{x, y, z\}} \hat{S}_{i,j} \otimes \hat{S}_{i,j}^T \right\} \quad (3.18)$$

k_{relax} is the relaxation rate constant and $\hat{S}_{i,j}$ is the spin-projection operator for the electron in radical i in the direction j . There are no experimental measurements for k_{relax} . However, estimates from molecular dynamics simulations and Bloch-Redfield relaxation theory suggests a value of at least $k_{relax} = 10^6 \text{ s}^{-1}$ [56]. For $k_{relax} \leq 10^5 \text{ s}^{-1}$ the protein would have to be either almost rigid or the radicals within it would have to undergo very rapid, very low, amplitude librational and torsional motions, neither of which are plausible [8]. This thesis uses $k_{relax} = 10^6 \text{ s}^{-1}$ for calculations where relaxation is included.

A full discussion regarding relaxation is beyond the scope of this thesis.

3.6 Liouville Space Calculation of Singlet Yield

The inclusion of kinetics (\hat{K}) and relaxation (\hat{W}) superoperators to the Liouville-von Neumann equation in Liouville space (Equation 2.29) results in Equation 3.19 as the equation describing the spin dynamics of the system.

$$\frac{d}{dt}\hat{\rho}(t) = -\hat{L}\hat{\rho}(t) \quad (3.19)$$

Where

$$\begin{aligned} \hat{L} &= i\hat{H} + \hat{K} + \hat{W} \\ &= i[\hat{H} \otimes \hat{\mathbb{1}} - \hat{\mathbb{1}} \otimes \hat{H}^T] + \frac{k_r}{2}[\hat{P}_s \otimes \hat{\mathbb{1}} + \hat{\mathbb{1}} \otimes \hat{P}_s^T] + k_f\hat{\mathbb{1}} \\ &\quad + k_{relax}\left\{\frac{3}{2}\hat{\mathbb{1}} + - \sum_{i \in \{FAD, W\}} \sum_{j \in \{x, y, z\}} \hat{S}_{i,j} \otimes \hat{S}_{i,j}^T\right\} \end{aligned} \quad (3.20)$$

The solution to Equation 3.19 for time-independent Hamiltonian, kinetics and relaxation superoperators is given in Equation 3.21:

$$\hat{\rho}(t) = \exp(-\hat{L}t)\hat{\rho}(0) \quad (3.21)$$

The solution in Equation 3.21 along with Equation 2.18 can be used to calculate the singlet probability at a given time t , $P_s(t)$.

$$P_s(t) = \text{Tr}[\hat{P}_s\hat{\rho}(t)] = \langle \hat{P}_s | e^{-\hat{L}t} | \hat{\rho}(0) \rangle \quad (3.22)$$

Equation 3.22 can be re-written as Equation 3.23 using the knowledge that all of the radicals start in the singlet ground state (GS), such that $\hat{\rho}(0) = \frac{1}{Z}\hat{P}_s$.

$$P_s(t) = \frac{1}{Z}\langle \hat{P}_s | e^{-\hat{L}t} | \hat{P}_s \rangle \quad (3.23)$$

Use of Equation 2.26 with Equation 3.23 allows for the calculation of Φ_s as:

$$\begin{aligned} \Phi_s &= \frac{k_r}{Z}\langle \hat{P}_s | e^{-\hat{L}t} | \hat{P}_s \rangle \\ &= \frac{k_r}{Z}\langle \hat{P}_s | \hat{L}^{-1} | \hat{P}_s \rangle \end{aligned} \quad (3.24)$$

The analogous Liouville space to a $n \times n$ Hilbert space has $n^2 \times n^2$ dimensions, which is represented by matrices that take up a factor of n^2 more bits. For the five-nuclear-spin case that is an increase in the memory requirement by a factor of 186,624. Due to the formal time-complexity of many essential operations such as matrix diagonalization being $\mathcal{O}(N^3)$ CPU-time becomes unpractical very quickly with the addition of more nuclear-spins.

3.7 The Flavin-Tryptophan Radical Pair

This section has been included as reference for the reader so that they are aware of which set of nuclear spins is involved in each simulation.

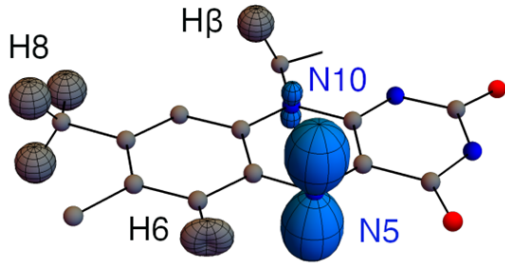


Figure 3.2: The seven biggest hyperfine couplings of FAD with labels. N for ^{14}N and H for ^1H . Figure reproduced with permission from their creator, Gediminas Pazera

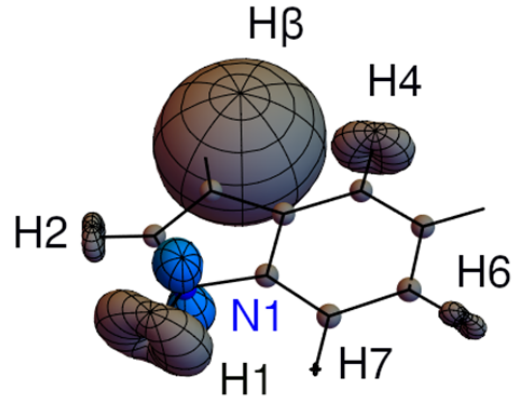


Figure 3.3: The seven biggest hyperfine couplings of $\text{Trp}_{C/D}$ with labels. N for ^{14}N and H for ^1H . Figure reproduced with permission from their creator, Gediminas Pazera

The calculations are built up by successively adding the nuclei with the biggest anisotropic hyperfine interactions. For the smallest spin-system, the three-nuclear-spin case, the nuclei included are the FAD N5 (Figure 3.2) and both of the Trp_C and Trp_D N1 nuclei (Figure 3.3). The five-nuclear-spin case is the same as the three-nuclear spin case, with the addition of both of the Trp_C and Trp_D H β nuclei (Figure 3.3). Any other nuclear spin systems will be discussed when necessary.

Equation 3.25 gives a measure of the effective anisotropic hyperfine interaction

of a radical, a_{eff} .

$$a_{eff} = \sqrt{\sum_{k=1}^N \sum_{j=1}^3 a_{kj}^2 I_k(I_k + 1)} \quad (3.25)$$

Where, a_{kj} and I_k are the eigenvalues ($j = 1, 2, 3$) of the hyperfine spin tensor and the spin quantum number of the nucleus k . N is the number of nuclear spins. The effective hyperfine interaction for a FAD-tryptophan radical pair is $a_{eff,FAD-Trp}$.

$$a_{eff,FAD-Trp} = \sqrt{(a_{eff,FAD})^2 + (a_{eff,Trp})^2} \quad (3.26)$$

Together there is a total of thirty ^1H and ^{14}N nuclei across the radical pair that make up the total anisotropic hyperfine interaction. Currently it is not possible to make realistic calculations that involve anywhere near all of these nuclei. However, use of [Equation 3.26](#) shows that the three and five nuclear-spin cases make up 64% and 69% of the total hyperfine interaction, respectively [8]. Therefore, it would appear to be a good approximation, that reasonably accurate calculations can be made with a small number of the most significantly anisotropic spins in the system.

3.8 Evaluation of Methods

The two methods outlined above in [section 3.4](#) and [section 3.6](#) both work out Φ_s . However, the Hilbert space method does not take into account any form of relaxation, which can only be valid if relaxation is not significant on the time scale on which singlet-triplet interconversion occurs. The benefits of working with the Hilbert space method are significantly reduced demands on memory and CPU-time, mentioned in [section 3.6](#). This allows for the addition of more nuclear-spins and the simulation of more data points in the same amount of time as analogous Liouville space calculations. The following section addresses the balance between the inclusion of different factors to produce the most ‘accurate’ simulations possible with the available machinery.

For clarity, it is important to define the term ‘accuracy’ in the context of this section:

Here, 'accuracy' refers to the extent to which a plot is realistic; a more reliable plot is a more accurate one. Therefore, the most accurate plots are those which include spin relaxation and are produced with as many data points and nuclear-spins as possible.

3.8.1 Results

All of the plots in this chapter are based on the cryptochrome system in migratory birds, using the composite RPM (Figure 3.1), so that any conclusions made are relevant to the rest of this thesis. The figures produced depict the relationship between signalling state anisotropy ($\Delta\Phi_{ss}$) and the proportion of RP1_C present in the total RP1 (f_C). To make the plots consistent with the expected electron transfer rates detailed in Figure 1.5 $k_{Cr} = 10^7 \text{ s}^{-1}$, $k_{Dr} = 10^5 \text{ s}^{-1}$ and $k_{Cf} \neq 0$ were chosen. These rates are different to those used by Wong *et al* in [8] which produced Figure 1.7, hence the slight differences in shape.

3.8.2 Number of Points

This section is broken into two sections. Firstly, the number of geomagnetic field directions over which Φ_{ss} is calculated to work out $\Delta\Phi_{ss}$. Secondly, the increment in f_C values in the range of $0 \leq f_C \leq 1$. Both sections aim to minimise the number of points required to get accurate results.

In [8], plots were made over 1600 evenly distributed geomagnetic field directions, over a full sphere, with the three-nuclear-spin case and relaxation (Figure 1.7). This has been used as a reference figure for what an 'accurate' simulation should look like. The f_C increment of 0.025 used in [8] will also be assessed.

Due to the lack of difference in the shape and features of the plots corresponding to the 1600 (red) and 100 (orange) geomagnetic field direction cases in Figure 3.4, it has been assumed that the 100 geomagnetic field direction's case is sufficiently

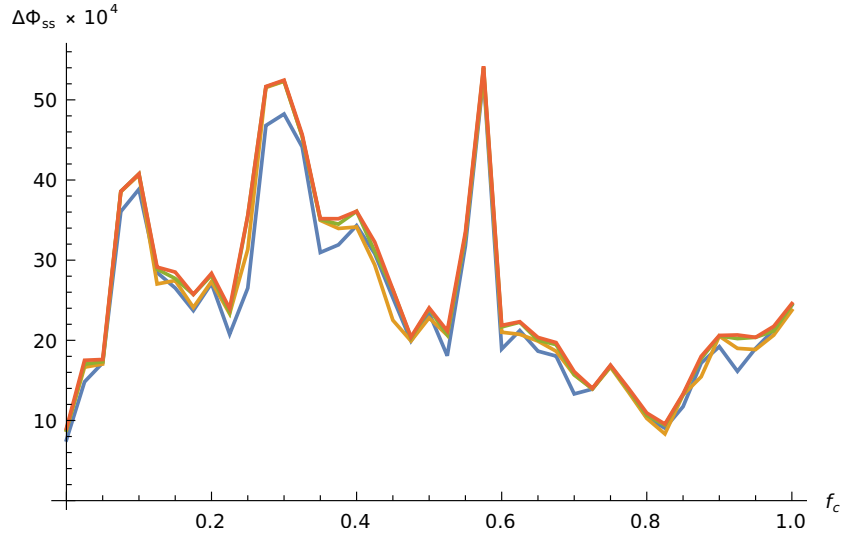


Figure 3.4: All lines have been made with three-nuclear-spin case (section 3.7) without relaxation. For all plots $k_{Cr} = 10^7 \text{ s}^{-1}$, $k_{Dr} = 10^5 \text{ s}^{-1}$ and $k_{Cf} = k_{Df} = 10^6 \text{ s}^{-1}$. The blue, orange, green and red plots correspond to the simulations being made over 64, 100, 400 and 1600 evenly-spaced geomagnetic field directions over a complete sphere, respectively. All calculations have been made with a f_C increment of 0.025.

accurate. This speeds up simulations by a factor of 16 compared to the 1600 field direction case (red). Plots with fewer field directions, such as the 64 direction case (blue), have a significant drop off in accuracy. In this thesis, plots will be made using 100 different field directions.

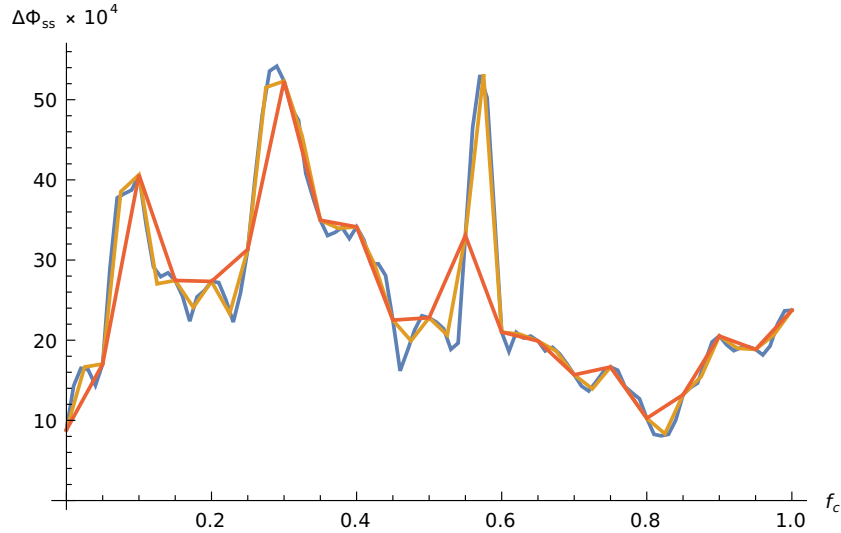


Figure 3.5: All plots have been made with three-nuclear-spin case (section 3.7), without relaxation. For all plots $k_{Cr} = 10^7 \text{ s}^{-1}$, $k_{Dr} = 10^5 \text{ s}^{-1}$ and $k_{Cf} = k_{Df} = 10^6 \text{ s}^{-1}$. The blue, yellow and orange lines have been made with a f_C increment of 0.01, 0.025 and 0.05, respectively. All plots have been made over 100 evenly-spaced geomagnetic field directions over a full sphere.

Figure 3.5 shows the effect of changing the increment by which the f_C value is varied. The accuracy of the simulations drops off significantly with an increment of less than 0.025. However, the plot with a f_C increment of 0.025 is very similar to the analogous one with an increment of 0.01. Therefore, the figures presented in this thesis have been made with an increment in f_C of 0.025, as in [8].

3.8.3 Number of Spins

Figure 3.6 shows the impact of adding nuclear-spins to the calculations. Spins are added in decreasing order of anisotropic hyperfine interactions (section 3.7).

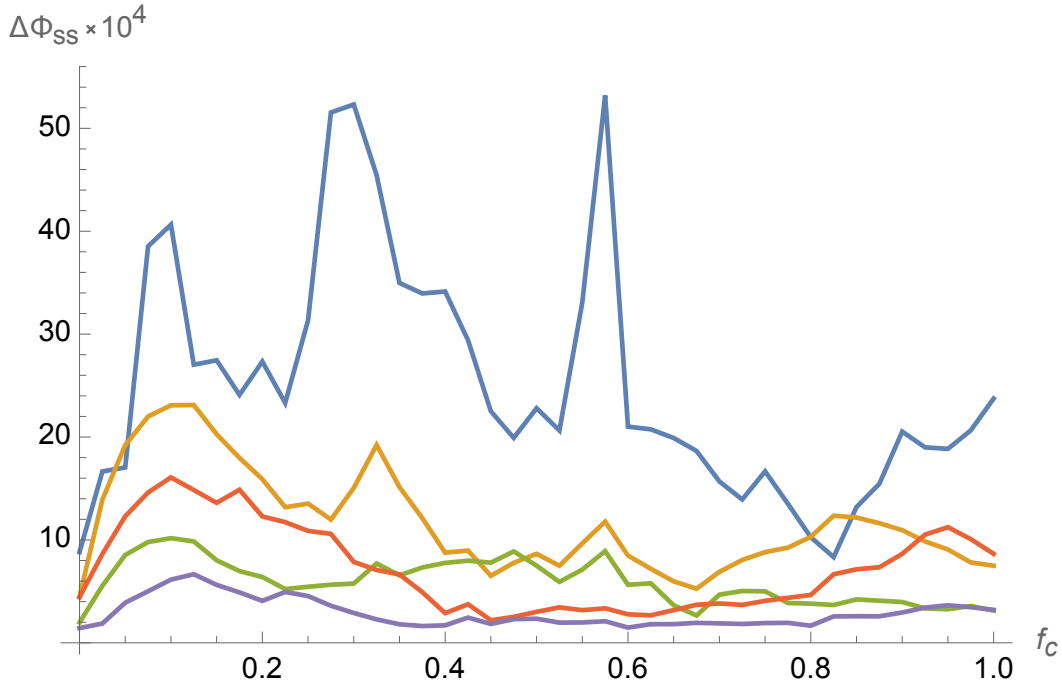


Figure 3.6: All plots have been made without relaxation, $k_{Cr} = 10^7 \text{ s}^{-1}$, $k_{Dr} = 10^5 \text{ s}^{-1}$ and $k_{Cf} = k_{Df} = 10^6 \text{ s}^{-1}$. The blue, yellow, green, orange and purple plots correspond to the three, five, six, seven and eight nuclear-spin cases, respectively. (See section 3.7 for reference to the different nuclear-spin cases.)

Figure 3.6 shows that, generally, the addition of nuclear-spins causes a reduction in the value of $\Delta\Phi_{ss}$, along with a change in the shape of the plot, $\Delta\Phi_{ss}$ - f_C relationship. As expected, the amount by which the key features of successive plots changes reduces as more, less anisotropic nuclear-spins are added. Therefore, it is expected that plots with significantly more nuclear-spins will resemble the plots produced

in Figure 3.6, all of which is inline with the mentioned diminishing returns gained by adding successive spins in section 3.7.

From Figure 3.6 it can be seen that all of the plots, apart from the three-nuclear-spin case, have relatively similar shapes, especially in the important $0 \leq f_C \leq 0.1$ region with which this thesis is concerned. ($0 \leq f_C \leq 0.1$ is the region of concern due to the finding made by Xu *et al.* that only f_C values ≤ 0.1 are consistent with experimental measurements [7]). This is due to the three-nuclear-spin case not including the H β protons on the typtophans that all of the other cases include (Figure 3.3). The conclusion that can be made from Figure 3.6 is that it is better to include as many spins as possible however, it is essential for this thesis that simulations are made with at least the five-nuclear-spin case, so that the H β nuclei are included.

All of the plots in Figure 3.6 have been made without relaxation in Hilbert space (section 3.4). This is because it is not practical to make plots with more than three-nuclear-spins and spin relaxation due to the increased demands associated with the use of Liouville space (section 3.6), which must be used if spin relaxation is included. The accuracy of this will be assessed in the following section.

3.8.4 Inclusion of Relaxation

Figure 3.7 shows that the impact of spin relaxation is to reduce the $\Delta\Phi_{ss}$ value and change the shape of the plots describing the relationship between $\Delta\Phi_{ss}$ and f_C .

Due to a lack of information regarding a minimum $\Delta\Phi_{ss}$ value required for the cryptochrome system to act as an effective magnetic compass sensor, the absolute accuracy of $\Delta\Phi_{ss}$ is not very meaningful. This can seem counter-intuitive due to the reduction in compass sensitivity ($\Delta\Phi_{ss}$) resulting from spin relaxation being one of the main problems facing the validity of the RPM in the cryptochrome system. However, due to the lack of relevance of the absolute value of $\Delta\Phi_{ss}$, it is the shape of the $\Delta\Phi_{ss}$ - f_C relationship that is important in aiding conclusions

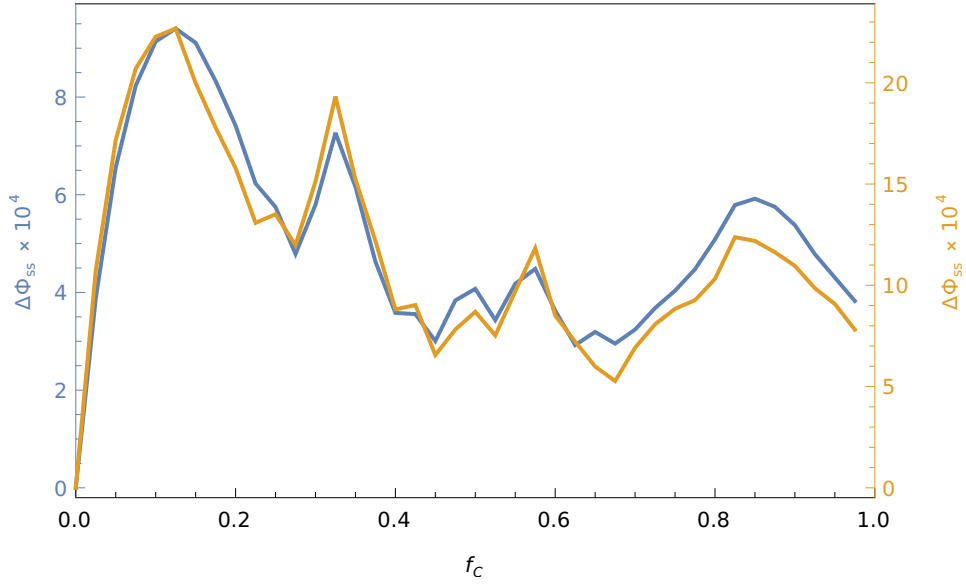


Figure 3.7: Both plots are produced with the five-nuclear-spin case (section 3.7), over 100 evenly spaced geomagnetic field directions, covering a complete sphere, with f_C values in increments of 0.025. The blue line is the reference plot with relaxation, and the orange line does not include relaxation. For both plots: $k_{Cr} = 10^7 \text{ s}^{-1}$, $k_{Dr} = 0 \text{ s}^{-1}$ and $k_{Cf} = k_{Df} = 10^6 \text{ s}^{-1}$. The blue and orange vertical axis correspond to the $\Delta\Phi_{ss}$ values for the (blue) reference plot with relaxation and the (orange) line without relaxation, respectively. The plots have been placed over one another with different scales so that the shape of the $\Delta\Phi_{ss}$ relationship can be easily assessed.

regarding the RPM in cryptochromes.

From Figure 3.7 it can be seen that spin relaxation only slightly alters the shape of the $\Delta\Phi_{ss}$ - f_C relationship, eventhough $\Delta\Phi_{ss}$ is reduced by a factor of 2.2 on average, suggesting that under the conditions that Figure 3.7 was calculated with, spin relaxation is not significantly important to the reliability of the conclusions made from singlet yield anisotropy plots.

Spin relaxation would only become more important if it becomes significantly faster on the time scale of the RP1 lifetime than it is in Figure 3.7. This would only be the case if k_{relax} is much faster than the expected 10^6 s^{-1} , or if the reaction rates are much slower than those predicted in Figure 1.5. There is no reason to suggest that a different number of nuclear-spins will drastically change the effect that spin relaxation

has; this is supported by the analogous three-nuclear-spin plot to [Figure 3.7](#), leading to the the same changes regarding the inclusion/exclusion of relaxation.

The small increase in how realistic – ‘accurate’ – the $\Delta\Phi_{ss}$ - f_C shapes are from the inclusion of relaxation, comes with a large CPU time and memory cost. This is due to the requirement for the use of Liouville space ([section 3.6](#)), instead of Hilbert space ([section 3.4](#)), to include relaxation. The size of the calculations in Liouville space compared to Hilbert space are significantly larger, the extent to which was discussed in [section 3.6](#), with Liouville space matrices analogous to the their Hilbert space counterparts taking up a factor of 186,624 more memory for the five-nuclear-spin case.

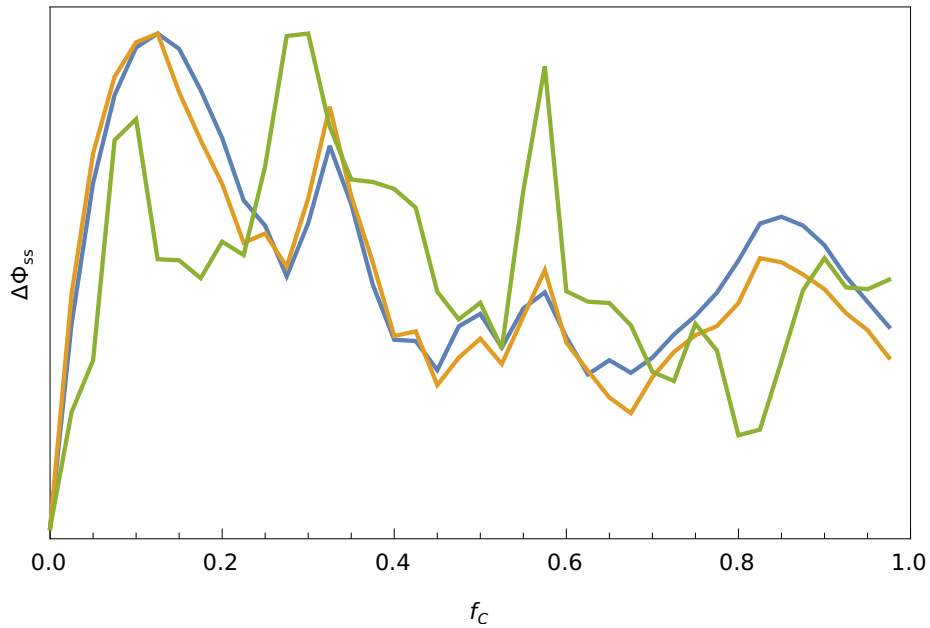


Figure 3.8: All plots are made using 100 equally spaced geomagnetic field directions, over a complete sphere, with an f_C increment of 0.025. The blue line is the reference plot with relaxation and the five-nuclear-spin case, the orange line was produced using the five-nuclear-spin case without relaxation and the green line with the three-nuclear-spin case with relaxation. For all plots: $k_{Cr} = 10^7 \text{ s}^{-1}$, $k_{Dr} = 0 \text{ s}^{-1}$ and $k_{Cf} = k_{Df} = 10^6 \text{ s}^{-1}$. I have not included the $\Delta\Phi_{ss}$ values in [Figure 3.8](#) due to the previous discussion about their lack of relevant importance. Note that the plots have been placed over one another and would all have largely different scales. This has been done so that the shape of the different plots can be easily compared. See [section 3.7](#) for a reference to the nuclear-spin cases.

Therefore, due to the large computational demands of this project, a choice

must be made between the three-nuclear-spin case with relaxation, or the five – or more – nuclear-spin case without relaxation.

In [subsection 3.8.3](#), it was concluded that inclusion of the H β nuclei was vital, due to the large change in the shape of the $\Delta\Phi_{ss}$ - f_C relationship upon their addition, which distinguished the three-nuclear-spin plot from the five – or more – nuclear-spin plots. From [Figure 3.8](#), it can be seen that the effect on the $\Delta\Phi_{ss}$ relationship due to the inclusion of the the H β nuclei drastically outweighs the impact of including relaxation.

This is concluded due to the reference, five-nuclear-spin case plot with relaxation, plot (blue) having a significantly more different $\Delta\Phi_{ss}$ - f_C relationship to the three-nuclear-spin case plot (green) with relaxation than that of the five-nuclear-spin case without relaxation (orange). Therefore, the plots in this thesis will be made without relaxation, but with the five – or more – nuclear-spin case.

Chapter 4

Validity of the Composite-Radical Pair Mechanism

Contents

4.1	Five Nuclear-Spin System	43
4.2	Higher-Spin Systems	49
4.3	Why Four Tryptophans Instead of Three?	51
4.4	Validity of Rate Constant Condition	52
4.5	Possibility of Expanding the Composite Model to Include Trp-B	53
4.6	Conclusions	53

The main argument discussing the validity of a composite RPM as the basis of a magnetic compass sense is laid out in [section 4.1](#) and [section 4.2](#). The rest of the chapter uses this to address the inconsistencies found by Xu *et al.* [7] mentioned in [chapter 1](#), along with the validity of the condition applied to the forward rate constant and the possibility of expanding the composite nature of the RP along the tryptophan chain.

4.1 Five Nuclear-Spin System

The set of results in this section have been made using the five-nuclear-spin system mentioned in [section 3.7](#) with $k_{Cr} = 10^7 \text{ s}^{-1}$, $k_{Dr} = 10^5 \text{ s}^{-1}$ and $k_{Cf} \equiv k_{Df} \equiv k_f$. The values of the rate constants chosen are based on the electron-transfer rates

presented in [Figure 1.5](#). The condition of $k_{Cf} \equiv k_{Df} \equiv k_f$ is valid and will be discussed in [section 4.4](#).

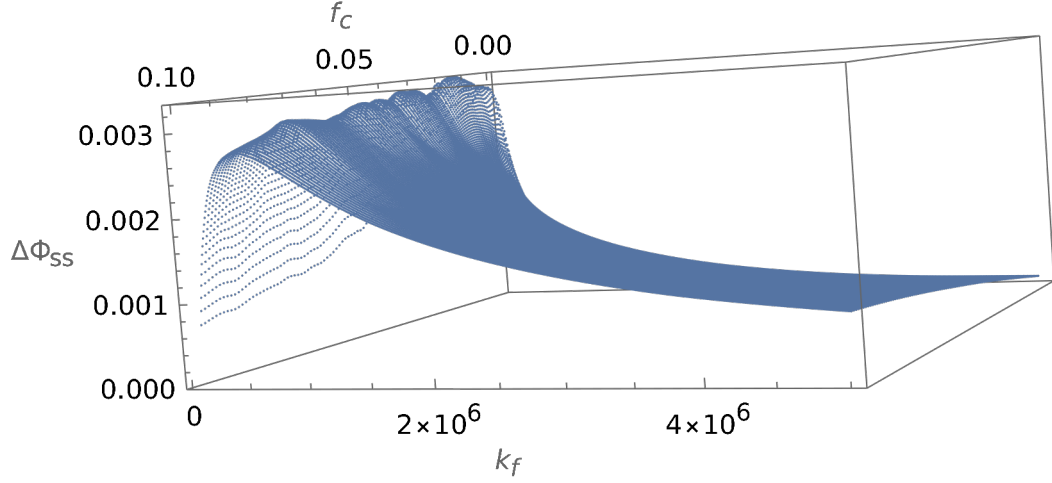


Figure 4.1: $\Delta\Phi_{ss}$ for the five-nuclear-spin composite RP with the variation of f_C and the forward rate constant which in this case is defined as $k_f \equiv k_{Cf} \equiv k_{Df}$. Note that $k_{Cr} = 10^7 \text{ s}^{-1}$ and $k_{Dr} = 10^5 \text{ s}^{-1}$ as from electron transfer rates in [Figure 1.5](#)

Increase in k_f^0 to a more physically reasonable value

Five-Nuclear-Spin System: Optimal Conditions for Different Models.

	Composite ($0 \leq f_C \leq 1$)	Conventional ($f_C = 0$)	Mutant ($f_C = 1$)
f_C^0	0.021	0.0	1.0
$k_f^0 \text{ (s}^{-1}\text{)}$	1.3×10^5	4.1×10^4	2.8×10^6
$\frac{k_r}{k_f^0}$	2.4	2.4	3.6

Table 4.1: A summary of the optimal conditions in [Figure 4.1](#), with k_f^0 and f_C^0 the values of k_f and f_C that, in combination, provide the greatest compass sensitivity ($\Delta\Phi_{ss}^0$). The data for the mutant case is from [Figure B.1](#) in [Appendix B](#).

[Table 4.1](#) shows that the optimal forward rate constant (k_f^0) for the composite RPM is an order of magnitude greater than for the conventional RPM. This can be explained by the two orders of magnitude difference between the conventional and mutant RPMs, which are the two extremes of the composite model. The large difference in optimal forward rate constant values for the two cases is expected due to the work by Xu *et al* [7]. It has been found that the system is optimised when $\frac{k_r}{k_f} \approx 3$ for k_f in the range of $10^5 - 10^8 \text{ s}^{-1}$. As $k_r = 10^5 \text{ s}^{-1}$ and 10^7 s^{-1} for the

conventional and mutant cases, respectively, it is clear that the optimal forward rate constants should also differ by two orders of magnitude, as they do. The bottom row of Table 4.1 shows that, for all of the models, the optimal $\frac{k_r}{k_f}$ ratio is consistent with the findings made by Xu *et al.* [7].

To 2.d.p the composite and conventional cases $\frac{k_r}{k_f^0}$ values are the same, which is expected due to the small 2% involvement of $RP1_C$ in the composite model when the system is optimised (see f_C^0 for the composite model). The small f_C^0 value is consistent with the findings made in [7] by Xu *et al.*, that $RP1_D$ is the dominant transient charge separated state in the wild-type protein. It is stated in [7] that f_C values up to 0.1 are consistent with the dipolar couplings measured for the wild-type *ErCry4*. This rules out the mutant case, with $f_C = 1$, as a contender for the biological system.

In the RP, the reactions must be competitive so that field-induced changes in the probabilities of the singlet and triplet states can change the fractions of the RPs that react by the two pathways and consequentially, the outcome of the reaction [6]. Therefore, it is important that neither k_f nor k_r dominate, which is why the optimal k_f value is within an order of magnitude of k_r , hence $\frac{k_r}{k_f} \approx 3$. It is also important that the overall reaction is not too fast, as this would result in there not being enough time for sufficient singlet-triplet interconversion under the Earth's magnetic field, leading to a lack of geomagnetic information being encoded into the product yields [6]. Both of these factors would reduce the sensitivity of the system as a magnetic compass and therefore, rule out very fast forward rate constants as the *in vivo* value. On the other hand, if the radical pair lifetime is too long, significant spin relaxation will occur and will result in the loss of compass sensitivity [6]. Studies have shown that on balance, a radical pair lifetime in the order of $1\mu s$ is optimal [6].

Little is known about the forward reaction; it is believed to be the non-spin selective deprotonation of the tryptophan radical cation [6–8]. This will have a rate pre-set by the *in vivo* conditions and the structure of the system involved. *In*

vitro measurements are available of the tryptophan radical cation deprotonation for several members of the Cry-photolyase superfamily, with their rate constants spanning four orders of magnitude ($10^6 - 10^{10} \text{ s}^{-1}$) [57–67].

Therefore, for the value of k_f to be physically reasonable for the application of a magnetic compass sensor, and consistent with previous measurements, it needs to be close to 10^6 s^{-1} . It is clear that the k_f^0 value of the composite RPM is more physically reasonable than that of the conventional RPM (Table 4.1). This provides support for the the composite RPM over the conventional RPM, which only involves one radical pair as the magnetic sensor.

Boost In Compass Sensitivity

Five-Nuclear-Spin System: Optimal Compass Sensitivity for Different Models.

	Composite ($0 \leq f_C \leq 1$)	Conventional ($f_C = 0$)	Mutant ($f_C = 1$)
$\Delta\Phi_{ss}^0 (\times 10^3)$	3.3	2.9	1.0
Boost	N/A	14%	230%

Table 4.2: A summary of the optimal compass sensitivity ($\Delta\Phi_{ss}^0$) of different models. Also shown is the % boost in optimal compass sensitivity provided by adopting the composite RPM for each model. The data for Table 4.2 is from Figure 4.1 and Figure B.1 in Appendix B for the mutant case.

The values in Table 4.2 have been computed using the optimal forward rate constant (k_f^0) for each case, as shown in Table 4.1. The optimised composite RPM compass sensitivity ($\Delta\Phi_{ss}^0$) is greater than that for the conventional RPM and mutant RPM. The composite RPM is the most sensitive mechanism. Due to the evolutionary pressure for the migratory birds to have as sensitive a magnetic compass sense as possible, this is strong evidence that the composite RPM is the correct mechanism.

The data in Table 4.2 does not disagree with the findings made by Xu *et al.*, that under *in vitro* conditions, the mutant case is more sensitive than the wild-type protein (composite/conventional RPM) [7]. The mutant case ($f_C = 1$) optimises systems where k_f is significantly larger than the value that optimises the composite

RPM (Figure 4.2). This is due to k_{Cr} being two orders of magnitude greater than k_{Dr} (Figure 1.5). Therefore, when k_f is large, the system will increase the f_C value in order to maintain the optimal condition of $\frac{k_r}{k_f^0} \approx 3$ [7]. The measurements made under *in vitro* conditions are likely to have been taken with larger than physically reasonable *in vivo* k_f values ($\approx 10^8 \text{ s}^{-1}$). Therefore, the simulations in this thesis are consistent with the experimental measurements.

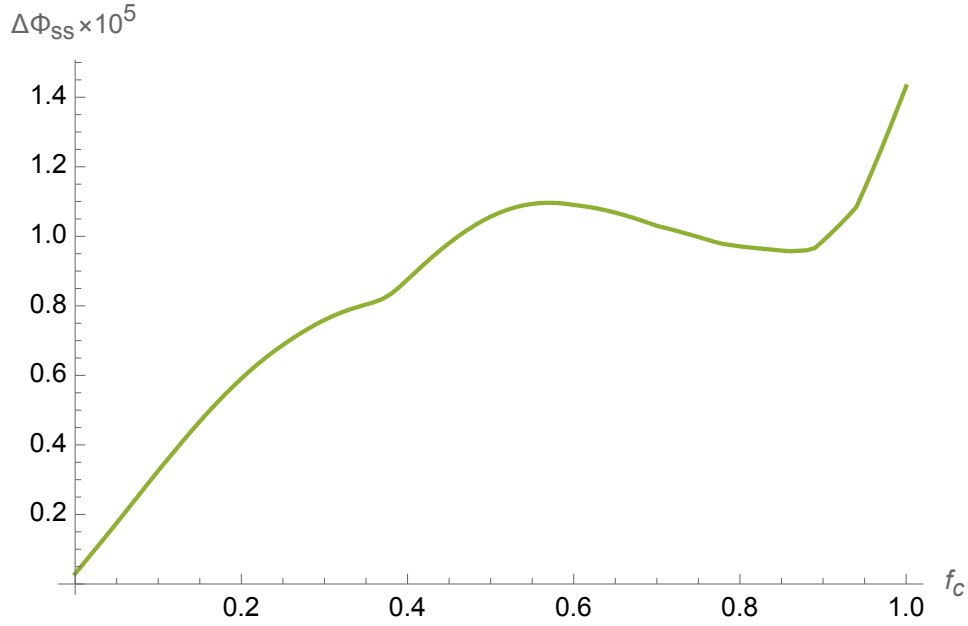


Figure 4.2: Signalling state yield anisotropy ($\Delta\Phi_{ss}$) against proportion of $RP1_C$ as the transient charge separated state in the cryptochrome (f_C), with $k_f = 10^8 \text{ s}^{-1}$. $k_{Cr} = 10^7 \text{ s}^{-1}$ and $k_{Dr} = 10^5 \text{ s}^{-1}$ as set by electron transfer rates listed in Figure 1.5

‘*In Vivo*’ Boost In Compass Sensitivity

It is clear from the previous discussion that the composite RPM is a more valid mechanism than the conventional RPM. This is due to both the more physically reasonable optimal forward rate constant, and the overall boost in compass sensitivity associated with adopting the composite RPM.

Due to the mentioned evolutionary pressure to develop the most sensitive possible magnetic compass sense, it is likely that the *in vivo* conditions are equal, or nearly equal, to the conditions that optimise the adopted composite RPM. Therefore,

setting k_f to the value that optimises the composite RPM gives a prediction of the *in vivo* boost provided by adopting the composite RPM.

Figure 4.3 shows the likely *in vivo* variation of compass sensitivity with f_C . Table 4.3 shows the likely boost in *in vivo* compass sensitivity due to adoption of the composite RPM over both the conventional RPM and mutant RPM.

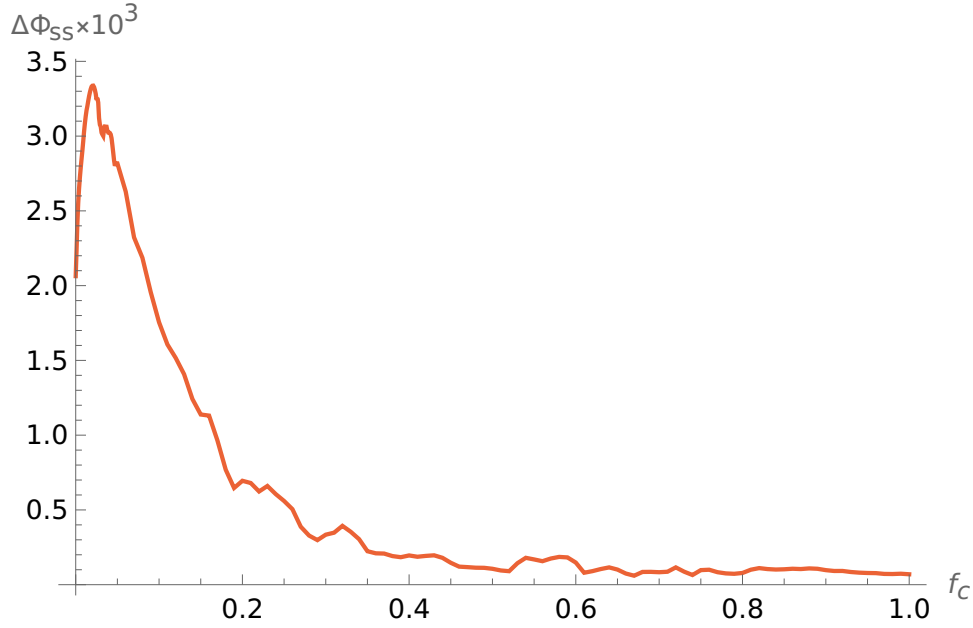


Figure 4.3: Signalling state yield anisotropy ($\Delta\Phi_{ss}$) against proportion of $RP1_C$ as the transient charge separated state in the cryptochrome (f_C) with $k_f = 1.3 \times 10^5 \text{ s}^{-1}$ such that the $\Delta\Phi_{ss}$ value is optimised at $f_C = 0.021$ (2.d.p). $k_{Cr} = 10^7 \text{ s}^{-1}$ and $k_{Dr} = 10^5 \text{ s}^{-1}$ as set by electron transfer rates listed in Figure 1.5.

Five-Nuclear-Spin System: ‘*In Vivo*’ Compass Sensitivity for Different Models.

	Composite ($0 \leq f_C \leq 1$)	Conventional ($f_C = 0$)	Mutant ($f_C = 1$)
$\Delta\Phi_{ss}^{I.V} \times 10^3$	3.3	2.1	0.070
I.V Boost	<i>N/A</i>	62%	4700%

Table 4.3: A summary of the ‘*in vivo*’ compass sensitivity ($\Delta\Phi_{ss}^{I.V}$) of different models. Also shown is the the % boost in ‘*in vivo*’ compass sensitivity provided by adopting the composite RPM for each model. The data for Table 4.3 is from Figure 4.3.

Due to the nature of the computer simulations in this thesis, it is likely that the numerical values given are not exact, but that the comparative boosts and shape of plots are accurate (chapter 3). Therefore, the data suggests that the composite RPM is indeed the mechanism behind the magnetic compass sense. If the *in vivo* rate

constant values were found to be close to the optimal values presented in Table 4.3, it would be strong evidence that Nature adopts the composite RPM.

4.2 Higher-Spin Systems

In chapter 3 it was shown that five-nuclear-spin case appears to be a minimum threshold required for calculations to resemble those made with larger nuclear-spin systems, which provide a more reliable picture of the system. This section aims to reproduce the figures made with five-nuclear-spin case in section 4.1 to check their reliability and ensure that they are not misleading.

Due to computational demands, a reduced number of data points has been used for the plots in this section, compared to section 4.1. The six – and seven – nuclear-spin cases are an extension of the five-nuclear-spin case (section 3.7). The six-nuclear-spin case includes the FAD N10 nitrogen (Figure 3.2). whilst, the seven-nuclear-spin case includes the H1 protons on Trp_C and Trp_D (Figure 3.3).

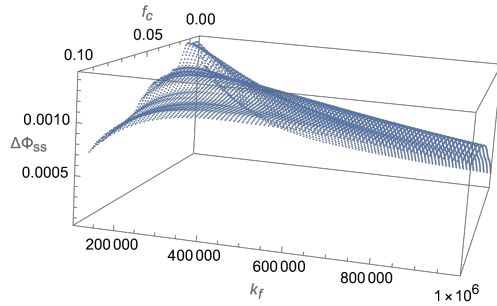


Figure 4.4: $\Delta\Phi_{ss}$ for the six-nuclear-spin system with the variation of f_C and the forward rate constant, which is defined as $k_f \equiv k_{Cf} \equiv k_{Df}$. $k_{Cr} = 10^7 \text{ s}^{-1}$ and $k_{Dr} = 10^5 \text{ s}^{-1}$ as from electron transfer rates in Figure 1.5

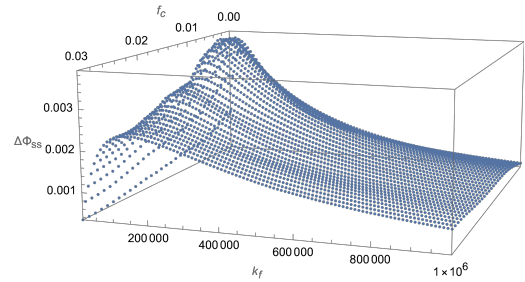


Figure 4.5: $\Delta\Phi_{ss}$ for the seven-nuclear-spin system with the variation of f_C and the forward rate constant, which is defined as $k_f \equiv k_{Cf} \equiv k_{Df}$. $k_{Cr} = 10^7 \text{ s}^{-1}$ and $k_{Dr} = 10^5 \text{ s}^{-1}$ as from electron transfer rates in Figure 1.5

Both Figure 4.4 and Figure 4.5 are in agreement with the five-nuclear-spin case (Figure 4.1). The same conclusion can be drawn from both, that the compass sensitivity is optimised by a non-zero f_C value significantly less than 0.1 (Table 4.4), in the region of $10^5 \text{ s}^{-1} \leq k_f \leq 10^6 \text{ s}^{-1}$. This provides further support for the

composite RPM as the overall findings are consistent, seemingly, independent of the number of nuclear-spins.

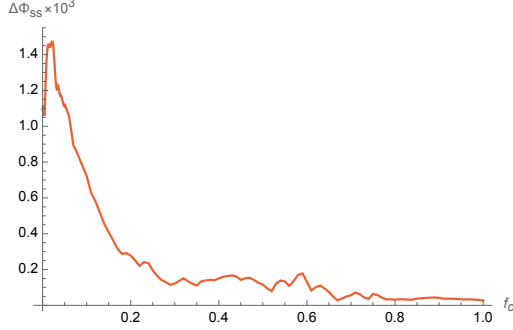


Figure 4.6: Six-nuclear-spin plot of the signalling state yield anisotropy ($\Delta\Phi_{ss}$) against proportion of $RP1_C$ as the transient charge separated state in the cryptochrome (f_C) with $k_f = 1.3 \times 10^5 \text{ s}^{-1}$, $k_{Cr} = 10^7 \text{ s}^{-1}$ and $k_{Dr} = 10^5 \text{ s}^{-1}$ as set by electron transfer rates listed in Figure 1.5.

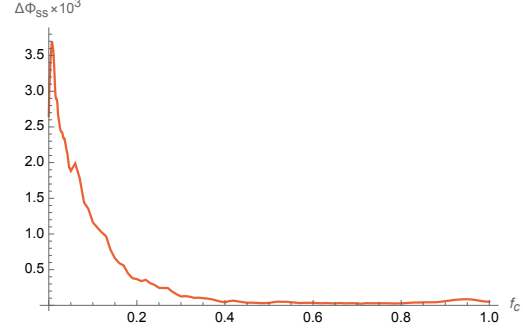


Figure 4.7: Seven-nuclear-spin plot of the signalling state yield anisotropy ($\Delta\Phi_{ss}$) against proportion of $RP1_C$ as the transient charge separated state in the cryptochrome (f_C) with $k_f = 1.3 \times 10^5 \text{ s}^{-1}$, $k_{Cr} = 10^7 \text{ s}^{-1}$ and $k_{Dr} = 10^5 \text{ s}^{-1}$ as set by electron transfer rates listed in Figure 1.5.

‘*In Vivo*’ Compass Sensitivity for Different Numbers of Nuclear-Spins.

	5-Nuclear-Spins	6-Nuclear-Spins	7-Nuclear-Spins
$f_C^{I.V.}$	0.021	0.021	0.0070
$\Delta\Phi_{ss}^{I.V.} \times 10^3$	3.3	1.5	3.7
I.V Boost	62%	35%	39%

Table 4.4: Summary of the ‘*in vivo*’ compass boost in sensitivity due to adopting the composite RPM over the conventional RPM for different numbers of nuclear-spins. Also shown is the optimal ‘*in vivo*’ compass sensitivity ($\Delta\Phi_{ss}^{I.V.}$), and the associated ‘*in vivo*’ f_C value ($f_C^{I.V.}$). The data for Table 4.4 is from Figure 4.3, Figure 4.6 and Figure 4.7.

As expected, due to subsection 3.8.3, the shape of all the plots in this section are consistent with the analogous plots in the five-nuclear-spin section (section 4.1). There is no reason to believe that the nature of the plots will drastically change as more, less significant, spins are added to the calculations. Therefore, it is safe to say that it can be expected that the composite RPM will also be favourable for the full *ErCy4* system as the basis for a magnetic compass sense.

4.3 Why Four Tryptophans Instead of Three?

The work presented in this chapter so far helps to answer the question posed by Wong *et al.* in [8] of ‘why might four tryptophans be better than three?’, which resulted from the finding made by Xu *et al.* that, *in vivo*, the three-tryptophan-based mutant sensor is more sensitive than the four-tryptophan-based wild type sensor (section 1.4) [7].

It appears that the answer to this question is likely due to two factors. One being the believed increased signalling ability of RP1_D (the fourth tryptophan) compared to RP1_C , due to the proximity of RP1_D to the surface of the cryptochrome and the neighboring Tyr319 residue (section 1.4) [7,8]. With the other reason being due to the apparent increased sensitivity that accompanies having two rapidly interconverting radical pairs (composite RPM) as opposed to a single radical pair.

This boost in sensitivity due to two rapidly interconverting radical pairs agrees with the suggestion made by Xu *et al.* but is not due to the suggested increased sensitivity of RP1_C over RP1_D (section 1.4) [7]. It was shown that only under large, unphysical, k_f values that the RP1_C three-tryptophan-based (mutant) RPM is more sensitive than the RP1_D four-tryptophan-based (conventional) RPM, showing that RP1_D is generally more sensitive than RP1_C .

Instead it showed that the four-tryptophan-based (conventional and composite) RPM gave a boost to compass sensitivity under more realistic, ‘*in vivo*’, k_f values, with the greatest compass sensitivity obtained with a four-tryptophan-based (composite) RPM. This is due to the greater flexibility of the system with the two rapidly interconverting radical pairs, providing Nature more opportunity to fine-tune the value of the overall rate constants, which seems to be the important factor in determining the sensitivity of the system to the Earth’s magnetic fields.

4.4 Validity of Rate Constant Condition

In [section 4.1](#) and [section 4.2](#) the condition of $k_{Cf} \equiv k_{Df} \equiv k_f$ has been used. This condition is applied to reduce the number of variables and hence the complexity of the system. This section aims to check the validity of this condition.

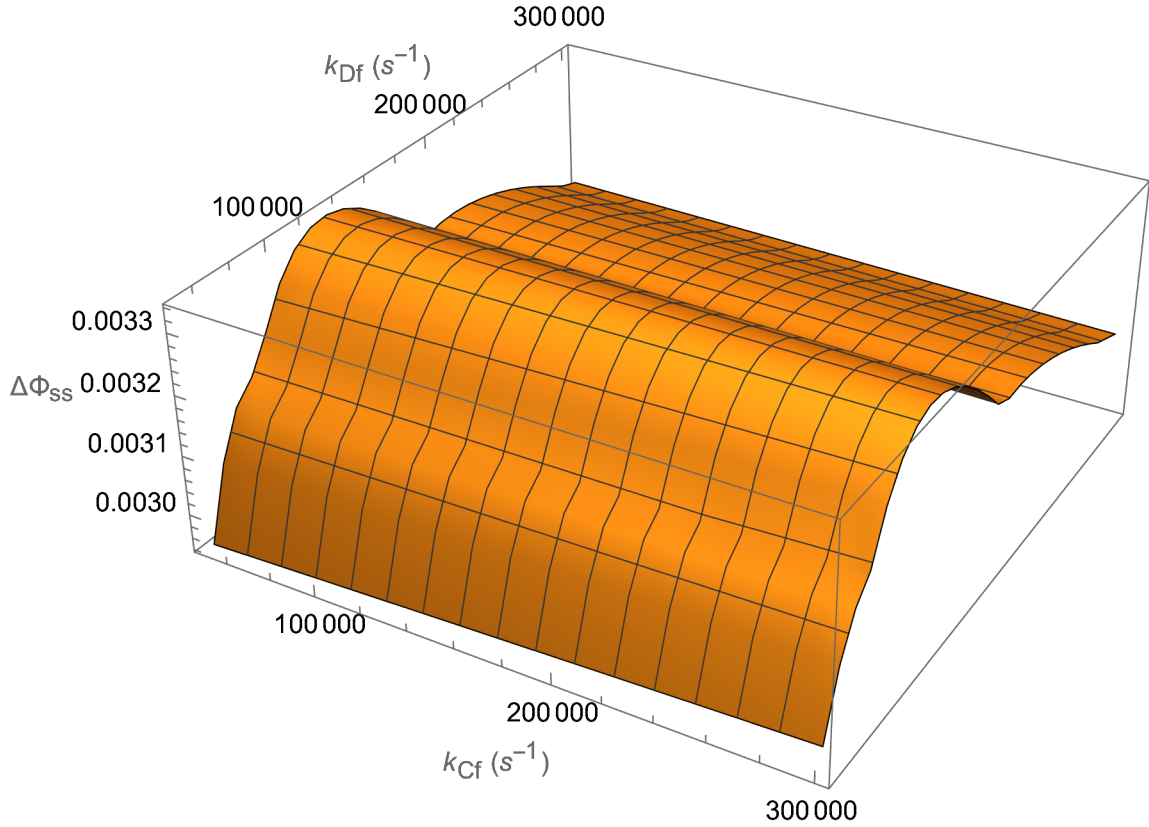


Figure 4.8: $\Delta\Phi_{ss}$ for the five-nuclear-spin composite system as a function of both k_{Cf} and k_{Df} . Each point has been calculated using the optimal f_C to provide the largest possible $\Delta\Phi_{ss}$

From [Figure 4.8](#) it is clear that there is little variation in compass sensitivity ($\Delta\Phi_{ss}$) with k_{Cf} , compared to the variation with k_{Df} . The optimal case in [Figure 4.8](#) does not satisfy the condition of $k_{Cf} \equiv k_{Df} \equiv k_f$. However, the difference in optimal compass sensitivity for the system with $k_{Cf} \neq k_{Df}$ is less than 1%. Such a small uncertainty is acceptable, as such a difference is likely to be unnoticeable to the birds.

It was expected that the variation of k_{Cf} would have an insignificant impact on the sensitivity of the system. This is because of the small (2% ([Table 4.1](#))) contribution

of k_{Cf} to the overall k_f value (Equation 3.4). The value of k_f is dominated by k_{Df} .

For this condition to become unphysical, a difference greater than an order of magnitude between k_{Cf} and k_{Df} would be needed. This is unlikely due to the close proximity of the two tryptophans, resulting in similar *in vivo* conditions, and due to their similar structure [7, 8].

4.5 Possibility of Expanding the Composite Model to Include Trp-B

A suggestion is that the composite nature of the RP could be extended further down the chain to include Trp_B (Figure 1.4). This would be with the hope of further increasing the optimal forward rate constant of the composite system to a more realistic one. However, due to the expected value of 10^6 s^{-1} for the backwards interconversion, from RP1_C to RP1_B (Figure 1.5), this is not the case. This is known due to the work by Wong *et al.*, which demonstrated that an interconversion rate in the order of 10^{10} s^{-1} is required to accurately model the system as a composite RP (Figure 1.7) [8].

There will be a small amount of RP1_C that interconverts back to RP1_B during the course of the reaction. However, due to the five orders of magnitude difference between the backwards and forwards rates of interconversion, any RP1_B formed will instantly interconvert back to RP1_C. As a result, Trp_B, and by extension Trp_A (Figure 1.4), will have little, or no, impact on the sensitivity of the system. Therefore, it is valid to exclude both Trp_B and Trp_A from calculations.

4.6 Conclusions

This chapter has provided evidence that the system with two rapidly interconverting radical pairs (composite RPM) can increase compass sensitivity compared to a system with a single radical pair (conventional/mutant RPM). This was shown to be due to

the greater flexibility in rate constants that can be achieved, allowing Nature increased opportunity to optimise the system as a magnetic sensor (section 4.1 and section 4.2).

It was also shown that adoption of the composite RPM over the conventional RPM leads to an increase in the value of the optimal forward rate constant to a more physically reasonable one. This makes the composite, two radical pair system, more physically reasonable than the conventional single radical pair system.

The findings from section 4.1 and section 4.2 were then used, along with a discussion of the signalling process, to help answer the question posed by Wong *et al.*: ‘Why Are Four Tryptophans Better Than Three?’ [8]. (Posed due to the finding in [7] that, *in vitro*, the altered (mutant) cryptochrome is more sensitive than the wild-type cryptochrome). It was concluded that this finding is not inconsistent with the cryptochrome being the site of a magnetic compass sensor, just that the result was most likely measured under conditions far from the *in vivo* environment for which the sensor is optimised.

The calculations presented in this thesis were made using the conditions of $k_{Cf} \equiv k_{Df} \equiv k_f$. Therefore, section 4.4 was required to assess the validity of this condition. It was found that the constraint is valid for the system due to the small variation of $\Delta\Phi_{ss}$ with k_{Cf} . This is due to the small $RP1_C$ contribution to $RP1$, of $\leq 10\%$ [7], resulting in the k_{Cf} value being irrelevant to the overall k_f value under the expected *in vivo* conditions.

In section 4.5, the possibility of expanding the composite nature of the RP along the tryptophan chain was discussed. Due to the backwards interconversion rate from $RP1_C$ to $RP1_B$ of 10^6 s^{-1} and the work by Wong *et al* [8], it was concluded that the composite nature is limited to $RP1_C$ and $RP1_D$. The section 4.5 also concluded that there is no need to include contributions from either $RP1_B$ or $RP1_A$ in the calculations of $\Delta\Phi_{ss}$, due to their short lifetimes.

Chapter 5

Conclusions and Future Work

In [chapter 3](#), it was concluded that the most realistic (‘accurate’) possible spin-dynamics calculations are those made with 5 – or more – nuclear-spins, without including spin relaxation. A choice had to be made between including relaxation and including the H β nuclei on Trp_C and Trp_D, due to computational demands. It was found that relaxation made less of a difference to the important $\Delta\Phi_{ss}$ - f_C relationship than the H β nuclei, hence the conclusion stated above, which is used throughout [chapter 4](#) to derive the following conclusions.

This thesis has provided evidence that the cryptochrome magnetic compass sensor can gain a boost in sensitivity by adopting a two-site (composite) RPM, over one with a single-site RP (conventional/mutant RPM). This is shown to be due to the greater flexibility in rate constants that can be achieved, allowing Nature increased opportunity to optimise the system as a magnetic sensor ([chapter 4](#)). See [section 3.1](#) for a complete definition of the various RPMs.

This finding was then used in [chapter 4](#), along with a discussion of the signalling process, to help answer the question posed by Wong *et al.*: ‘Why Are Four Tryptophans Better Than Three?’ [8]. This question was posed due to the finding in [7] that, *in vitro*, the altered (mutant) cryptochrome is more sensitive than the wild-type cryptochrome. It was concluded that this finding is not inconsistent with the cryptochrome being the site of a magnetic compass sensor, just that the

result was most likely measured under conditions far from the *in vivo* environment where the sensor is optimised.

In [chapter 4](#), it was also shown that the adoption of the modified (two-site) composite RPM over the previously accepted [\[6\]](#) (one-site) conventional RPM leads to an increase in the value of the optimal forward rate constant to a more physically reasonable one. This finding makes the composite RPM more physically reasonable than the conventional RPM. It was also explained why the composite nature of the RP is limited to the inclusion of Trp_C and Trp_D .

Due to these conclusions, this thesis suggests that the two-site (composite) RP in the cryptochrome is, to date, the most suitable magnetic compass sensor for migratory birds. To provide further confidence in this conclusion further work is required.

The most useful evidence for proving/disproving the conclusions in this thesis is the measurement of *in vivo* values for the forward rate constant, and a greater understanding of the forward reactions and signalling process as a whole. These values need to come from experiments; the greater understanding of the forward reaction and signalling process could come from modelling of the Tyr319 residue (introduced in [section 1.4](#)) and its interactions with the system.

A piece of work capable of largely improving the validity of the conclusions made by spin dynamics simulations of the cryptochrome system, in a quantitative way, is the calculation of a minimum compass sensitivity ($\Delta\Phi_{ss}^{Min}$). $\Delta\Phi_{ss}^{Min}$ would be the minimum value required for the birds to feasibly use the system as a magnetic compass sense. Again, this would require greater knowledge of the forward reaction and also the signalling process as a whole.

Clearly, the development of computational programs and hardware, along with new methods, is a key area of future work which would allow for the development of more realistic simulations

Bibliography

- [1] Berthold, P. *et al.* Der zug des weißstorchs (*ciconia ciconia*): eine besondere zugform auf grund neuer ergebnisse. *Journal für Ornithologie* **142**, 73–92 (2001).
- [2] Wikimedia commons. creative commons licence (2022). URL <https://en.wikipedia.org/wiki/Pfeilstorch%3aLambdaPlaques.jpg>.
- [3] Wiltschko, W. Über den einfluß statischer magnetfelder auf die zugorientierung der rotkehlchen (*erithacus rubecula*). *Zeitschrift für Tierpsychologie* **25**, 537–558 (1968).
- [4] Merkel, F. W. & Wiltschko, W. Magnetismus und richtungsfinden zugunruhiger rotkehlchen (*erithacus rubecula*). *Vogelwarte* **23**, 71–77 (1965).
- [5] Mouritsen, H. Long-distance navigation and magnetoreception in migratory animals. *Nature* **558** (2018).
- [6] Hore, P. J. & Mouritsen, H. The radical-pair mechanism of magnetoreception. *Annual Review of Biophysics* **45**, 299–344 (2016).
- [7] Xu, J. *et al.* Magnetic sensitivity of cryptochrome 4 from a migratory songbird. *Nature* **594**, 535–540 (2021).
- [8] Wong, S. Y., Wei, Y., Mouritsen, H., Solov'yov, I. A. & Hore, P. Cryptochrome magnetoreception: four tryptophans could be better than three. *Journal of the Royal Society Interface* **18**, 20210601 (2021).
- [9] Wong, S. Y. *et al.* Navigation of migratory songbirds: a quantum magnetic compass sensor. *Neuroforum* **27**, 141–150 (2021).
- [10] Mouritsen, H. Navigation in birds and other animals. *Image and Vision Computing* **19**, 713–731 (2001).
- [11] Wiltschko, W. & Wiltschko, R. Magnetic compass of european robins. *Science* **176**, 62–64 (1972).
- [12] Wiltschko, W. & Wiltschko, R. Magnetic orientation in birds. *The Journal of Experimental Biology* **199**, 29–38 (1996).
- [13] Åkesson, S., Morin, J., Muheim, R. & Ottosson, U. Avian orientation at steep angles of inclination: experiments with migratory white-crowned sparrows at the magnetic north pole. *Proceedings of the Royal Society of London. Series B: Biological Sciences* **268**, 1907–1913 (2001).
- [14] Lefeldt, N., Dreyer, D., Schneider, N.-L., Steenken, F. & Mouritsen, H. Migratory blackcaps tested in emlen funnels can orient at 85 degrees but not at 88 degrees magnetic inclination. *Journal of Experimental Biology* **218**, 206–211 (2015).
- [15] Engels, S. *et al.* Anthropogenic electromagnetic noise disrupts magnetic compass orientation in a migratory bird. *Nature* **509**, 353–356 (2014).
- [16] Ritz, T., Thalau, P., Phillips, J. B., Wiltschko, R. & Wiltschko, W. Resonance effects indicate a radical-pair mechanism for avian magnetic compass. *Nature* **429**, 177–180 (2004).

- [17] Ritz, T. *et al.* Magnetic compass of birds is based on a molecule with optimal directional sensitivity. *Biophysical journal* **96**, 3451–3457 (2009).
- [18] Schwarze, S. *et al.* Weak broadband electromagnetic fields are more disruptive to magnetic compass orientation in a night-migratory songbird (*erithacus rubecula*) than strong narrow-band fields. *Frontiers in behavioral neuroscience* **10**, 55 (2016).
- [19] Thalau, P., Ritz, T., Stapput, K., Wiltshko, R. & Wiltshko, W. Magnetic compass orientation of migratory birds in the presence of a 1.315 mhz oscillating field. *Naturwissenschaften* **92**, 86–90 (2005).
- [20] Mouritsen, H. *The Magnetic Senses*, 427–443 (Springer Berlin Heidelberg, Berlin, Heidelberg, 2013).
- [21] Mouritsen, H. *Magnetoreception in birds and its use for long-distance migration*, 113–133 (Elsevier, New York, 2014).
- [22] Wiltshko, R. & Wiltshko, W. Magnetic orientation in animals, springer-verlag, berlin. 1995. *Journal of Navigation* **49**.
- [23] Johnsen, S. & Lohmann, K. J. The physics and neurobiology of magnetoreception. *Nature Reviews Neuroscience* **6**, 703–712 (2005).
- [24] Mora, C. V., Davison, M., Martin Wild, J. & Walker, M. M. Magnetoreception and its trigeminal mediation in the homing pigeon. *Nature* **432**, 508–511 (2004).
- [25] Beason, R. & Semm, P. Does the avian ophthalmic nerve carry magnetic navigational information? *The Journal of experimental biology* **199**, 1241–1244 (1996).
- [26] Zapka, M. *et al.* Visual but not trigeminal mediation of magnetic compass information in a migratory bird. *Nature* **461**, 1274–1277 (2009).
- [27] Kishkinev, D., Chernetsov, N., Heyers, D. & Mouritsen, H. Migratory reed warblers need intact trigeminal nerves to correct for a 1,000 km eastward displacement. *PLoS One* **8**, e65847 (2013).
- [28] Schulten, K., Swenberg, C. E. & Weller, A. A biomagnetic sensory mechanism based on magnetic field modulated coherent electron spin motion. *Zeitschrift für Physikalische Chemie* **111**, 1–5 (1978).
- [29] Schulten, K. & Windemuth, A. Model for a physiological magnetic compass. *Biophysical effects of steady magnetic fields* **11**, 99–106 (1986).
- [30] Rodgers, C. T. & Hore, P. J. Chemical magnetoreception in birds: The radical pair mechanism. *Proceedings of the National Academy of Sciences* **106**, 353–360 (2009).
- [31] Gerlach, W. & Stern, O. Der experimentelle nachweis der richtungsquantelung im magnetfeld. *Zeitschrift für Physik* **9**, 349–352 (1922).
- [32] Timmel, C., Till, U., Brocklehurst, B., Mclauchlan, K. & Hore, P. Effects of weak magnetic fields on free radical recombination reactions. *Molecular Physics* **95**, 71–89 (1998).
- [33] Finlay, C. C. *et al.* International geomagnetic reference field: the eleventh generation. *Geophysical Journal International* **183**, 1216–1230 (2010).
- [34] Lewis, A. Spin dynamics in radical pairs, phd thesis, university of oxford, 2017 .
- [35] Maeda, K. *et al.* Chemical compass model of avian magnetoreception. *Nature* **453**, 387–390 (2008).
- [36] Rodgers, C. T. Magnetic field effects in chemical systems. *Pure and Applied Chemistry* **81**, 19–43 (2009).
- [37] Timmel, C., Cintolesi, F., Brocklehurst, B. & Hore, P. Model calculations of magnetic field effects on the recombination reactions of radicals with anisotropic hyperfine interactions. *Chemical physics letters* **334**, 387–395 (2001).

- [38] Ritz, T., Adem, S. & Schulten, K. A model for photoreceptor-based magnetoreception in birds. *Biophysical journal* **78**, 707–718 (2000).
- [39] Karki, N., Vergish, S. & Zoltowski, B. D. Cryptochromes: photochemical and structural insight into magnetoreception. *Protein Science* **30**, 1521–1534 (2021).
- [40] Wu, H., Scholten, A., Einwich, A., Mouritsen, H. & Koch, K.-W. Protein-protein interaction of the putative magnetoreceptor cryptochrome 4 expressed in the avian retina. *Scientific reports* **10**, 1–13 (2020).
- [41] Zoltowski, B. D. *et al.* Chemical and structural analysis of a photoactive vertebrate cryptochrome from pigeon. *Proceedings of the National Academy of Sciences* **116**, 19449–19457 (2019).
- [42] Giovani, B., Byrdin, M., Ahmad, M. & Brettel, K. Light-induced electron transfer in a cryptochrome blue-light photoreceptor. *Nature Structural & Molecular Biology* **10**, 489–490 (2003).
- [43] Günther, A. *et al.* Double-cone localization and seasonal expression pattern suggest a role in magnetoreception for european robin cryptochrome 4. *Current Biology* **28**, 211–223 (2018).
- [44] Schmied, R. Using mathematica for quantum mechanics (2020).
- [45] Fano, U. Description of states in quantum mechanics by density matrix and operator techniques. *Rev. Mod. Phys.* **29**, 74–93 (1957).
- [46] Ernst, R. R., Bodenhausen, G. & Wokaun, A. *Principles of nuclear magnetic resonance in one and two dimensions*, vol. 14 (Clarendon press Oxford, 1987).
- [47] Hore, P. J., Jones, J. A. & Wimperis, S. *NMR: The toolkit: How pulse sequences work*, vol. 92 (Oxford University Press, USA, 2015).
- [48] Rodgers, C. T. & Hore, P. J. Chemical magnetoreception in birds: The radical pair mechanism. *Proceedings of the National Academy of Sciences* **106**, 353–360 (2009).
- [49] Haberkorn, R. Density matrix description of spin-selective radical pair reactions. *Molecular Physics* **32**, 1491–1493 (1976).
- [50] Jones, J. A. & Hore, P. J. Spin-selective reactions of radical pairs act as quantum measurements. *Chemical Physics Letters* **488**, 90–93 (2010).
- [51] Kominis, I. K. Quantum theory of radical-ion-pair recombination: a new physical paradigm for low-magnetic-field effects. *arXiv preprint arXiv:0805.3081* (2008).
- [52] Kominis, I. K. Quantum zeno effect explains magnetic-sensitive radical-ion-pair reactions. *Physical Review E* **80**, 056115 (2009).
- [53] Kominis, I. K. Radical-ion-pair reactions are the biochemical equivalent of the optical double-slit experiment. *Physical Review E* **83**, 056118 (2011).
- [54] Lau, J. Spin-selective chemical reactions in radical pair magnetoreception, phd thesis, university of oxford, 2014 .
- [55] Kattnig, D. R., Sowa, J. K., Solov'yov, I. A. & Hore, P. Electron spin relaxation can enhance the performance of a cryptochrome-based magnetic compass sensor. *New Journal of Physics* **18**, 063007 (2016).
- [56] Kattnig, D. R., Solov'yov, I. A. & Hore, P. Electron spin relaxation in cryptochrome-based magnetoreception. *Physical Chemistry Chemical Physics* **18**, 12443–12456 (2016).
- [57] Maeda, K. *et al.* Magnetically sensitive light-induced reactions in cryptochrome are consistent with its proposed role as a magnetoreceptor. *Proceedings of the National Academy of Sciences* **109**, 4774–4779 (2012).

- [58] Müller, P., Yamamoto, J., Martin, R., Iwai, S. & Brettel, K. Discovery and functional analysis of a 4th electron-transferring tryptophan conserved exclusively in animal cryptochromes and (6-4) photolyases. *Chemical Communications* **51**, 15502–15505 (2015).
- [59] Immeln, D., Weigel, A., Kottke, T. & Perez Lustres, J. L. Primary events in the blue light sensor plant cryptochrome: intraprotein electron and proton transfer revealed by femtosecond spectroscopy. *Journal of the American Chemical Society* **134**, 12536–12546 (2012).
- [60] Müller, P., Ignatz, E., Kiontke, S., Brettel, K. & Essen, L.-O. Sub-nanosecond tryptophan radical deprotonation mediated by a protein-bound water cluster in class ii dna photolyases. *Chemical science* **9**, 1200–1212 (2018).
- [61] Lacombat, F. *et al.* Delocalized hole transport coupled to sub-ns tryptophanyl deprotonation promotes photoreduction of class ii photolyases. *Physical Chemistry Chemical Physics* **20**, 25446–25457 (2018).
- [62] Aubert, C., Vos, M. H., Mathis, P., Eker, A. P. & Brettel, K. Intraprotein radical transfer during photoactivation of dna photolyase. *Nature* **405**, 586–590 (2000).
- [63] Byrdin, M. *et al.* Intraprotein electron transfer and proton dynamics during photoactivation of dna photolyase from e. coli: Review and new insights from an “inverse” deuterium isotope effect. *Biochimica et Biophysica Acta (BBA)-Bioenergetics* **1655**, 64–70 (2004).
- [64] Byrdin, M. *et al.* Quantum yield measurements of short-lived photoactivation intermediates in dna photolyase: toward a detailed understanding of the triple tryptophan electron transfer chain. *The Journal of Physical Chemistry A* **114**, 3207–3214 (2010).
- [65] Müller, P. *et al.* Atp binding turns plant cryptochrome into an efficient natural photoswitch. *Scientific Reports* **4**, 1–11 (2014).
- [66] Paulus, B. *et al.* Spectroscopic characterization of radicals and radical pairs in fruit fly cryptochrome—protonated and nonprotonated flavin radical-states. *The FEBS journal* **282**, 3175–3189 (2015).
- [67] Kutta, R. J., Archipowa, N. & Scrutton, N. S. The sacrificial inactivation of the blue-light photosensor cryptochrome from drosophila melanogaster. *Physical Chemistry Chemical Physics* **20**, 28767–28776 (2018).

Appendices

Appendix A

Hyperfine and Dipolar Tensors

A.1 Hyperfine Tensors

Below are the hyperfine tensors for $\text{FAD}^{\bullet+}$ and $\text{Trp}_C\text{H}^{\bullet-}$ and $\text{Trp}_D\text{H}^{\bullet-}$ radicals used to produce spin dynamics of the cryptochrome system (in [Table A.1](#), [Table A.2](#) and [Table A.3](#), respectively). The tensors were calculated using density functional theory in Gaussian-03 at the UB3LYP/EPR-III level by Ilya Kuprov.

The labels for nuclei correspond to those given in [Figure A.1](#) and [Figure A.2](#).

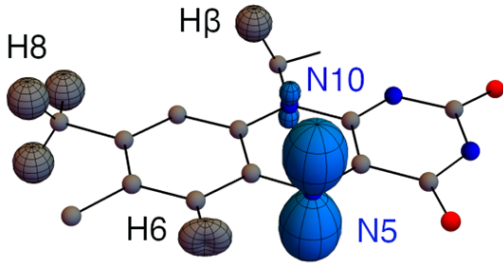


Figure A.1: The seven biggest hyperfine couplings of FAD with labels. N for ^{14}N and H for ^1H . Figure reproduced with permission from their creator, Gediminas Pazera

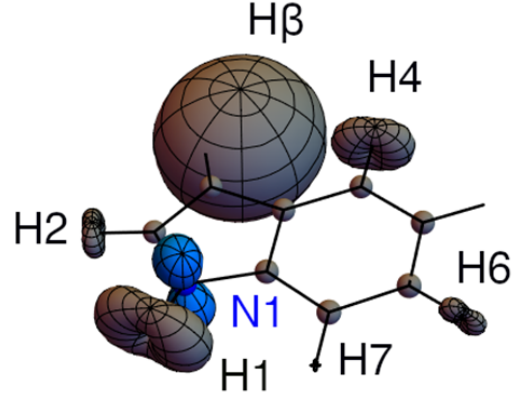


Figure A.2: The seven biggest hyperfine couplings of $\text{Trp}_{C/D}$ with labels. N for ^{14}N and H for ^1H . Figure reproduced with permission from their creator, Gediminas Pazera.

A.2 Dipolar Tensors

D_C and D_D are the dipolar tensor between $\text{FAD}^{\bullet+}$ with $\text{Trp}_C\text{H}^{\bullet-}$ and $\text{Trp}_D\text{H}^{\bullet-}$, respectively in MHz ([Equation A.1](#)). The dipolar tensors have been calculated and provided by P. J. Hore [\[6\]](#).

$$D_C = \begin{pmatrix} 1.090 & -12.121 & 4.905 \\ -12.121 & -7.802 & 7.024 \\ 4.905 & 7.024 & 6.712 \end{pmatrix} D_D = \begin{pmatrix} 2.417 & -6.154 & 1.412 \\ -6.154 & -7.176 & 2.890 \\ 1.412 & 2.890 & 4.760 \end{pmatrix} \quad (\text{A.1})$$

Hyperfine Tensors in the $\text{FAD}^{\bullet+}$ Radical

Nucleus	Hyperfine Tensor (MHz)
N5	$\begin{pmatrix} -2.787 & -0.080 & 0 \\ -0.080 & -2.451 & 0 \\ 0 & 0 & 49.237 \end{pmatrix}$
N10	$\begin{pmatrix} -0.416 & -0.058 & 0 \\ -0.058 & -0.664 & 0 \\ 0 & 0 & 16.944 \end{pmatrix}$

Table A.1: Hyperfine Tensors in the $\text{FAD}^{\bullet+}$ Radical.Hyperfine Tensors in the $\text{Trp}_C\text{H}^{\bullet-}$ Radical

Nucleus	Hyperfine Tensor (MHz)
N5	$\begin{pmatrix} -1.484 & 1.644 & -1.290 \\ 1.644 & 15.819 & -15.828 \\ -1.290 & -15.828 & 12.699 \end{pmatrix}$
H β	$\begin{pmatrix} -28.050 & 5.778 & 5.416 \\ 5.778 & -12.375 & 8.612 \\ 5.416 & 8.612 & -9.878 \end{pmatrix}$
H1	$\begin{pmatrix} 44.055 & 0.439 & 1.330 \\ 0.439 & 42.489 & 1.767 \\ 1.330 & 1.767 & 48.360 \end{pmatrix}$

Table A.2: Hyperfine Tensors in the $\text{Trp}_C\text{H}^{\bullet-}$ Radical.Hyperfine Tensors in the $\text{Trp}_D\text{H}^{\bullet-}$ Radical

Nucleus	Hyperfine Tensor (MHz)
N5	$\begin{pmatrix} -1.774 & 0.395 & 0.022 \\ 0.395 & 29.817 & 3.871 \\ 0.022 & 3.871 & -1.008 \end{pmatrix}$
H β	$\begin{pmatrix} -19.530 & 1.735 & -14.347 \\ 1.735 & -19.791 & -0.742 \\ -14.347 & -0.742 & -11.053 \end{pmatrix}$
H1	$\begin{pmatrix} 44.868 & 2.016 & -1.778 \\ 2.016 & 43.803 & -2.373 \\ -1.778 & -2.373 & 46.241 \end{pmatrix}$

Table A.3: Hyperfine Tensors in the $\text{Trp}_D\text{H}^{\bullet-}$ Radical.

Appendix B

Mutant RPM Figure

Figure B.1 shows the data from which Table 4.1 was made. For comparison to the conventional RPM the analogous Figure B.2 has been included.

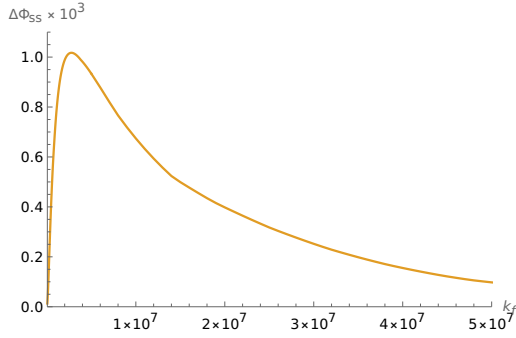


Figure B.1: Signalling state anisotropy ($\Delta\Phi_{ss}$) against the value of the forward rate constant (k_f in s^{-1}) for the mutant RPM. To be consistent with calculated rates in [7] $k_r = 10^7 \text{ s}^{-1}$.

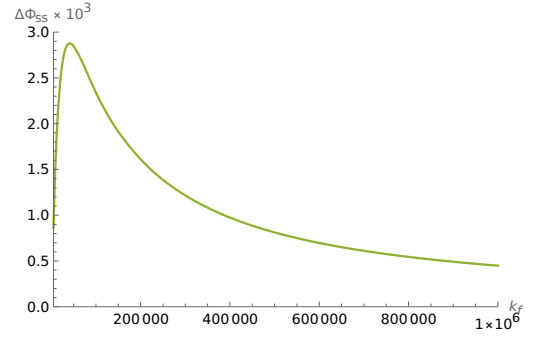


Figure B.2: Signalling state anisotropy ($\Delta\Phi_{ss}$) against the value of the forward rate constant (k_f in s^{-1}) for the conventional RPM. To be consistent with calculated rates in [7] $k_r = 10^5 \text{ s}^{-1}$.

Comparison of the two figures shows that the two orders of magnitude difference between the optimal forward rate constants (k_f^0) between the two models, as presented in Table 4.1.